J. Fluid Mech. (2025), *vol.* 1023, A12, doi:10.1017/jfm.2025.10786

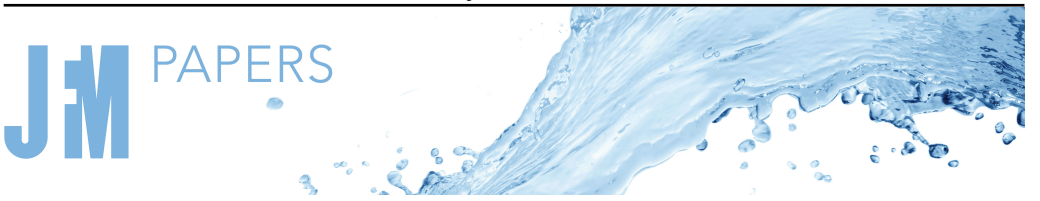

Fourier-based proper orthogonal decomposition of a turbulent round jet

Vivek Mugundhan[1,2], **Tiernan Casey**[1], **Jun Sakakibara**[3], **Peter J. Schmid**[1] and **S.T. Thoroddsen**[1]

[1]Division of Physical Sciences and Engineering, King Abdullah University of Science and Technology (KAUST), Thuwal 23955-6900, Saudi Arabia

[2]Department of Mechanical Engineering, Amrita School of Engineering Coimbatore, Amrita Vishwa Vidyapeetham, Coimbatore, India

[3]Department of Mechanical Engineering, Meiji University, Kawasaki, Japan

Corresponding author: Peter J. Schmid, peter.schmid@kaust.edu.sa

(Received 25 March 2025; revised 9 September 2025; accepted 26 September 2025)

We use scanning-tomographic particle image velocimetry introduced by Casey, Sakakibara & Thoroddsen (*Phys. Fluids,* vol. 25 (2), 2013, p. 025102) to measure the volumetric velocity field in a fully turbulent round jet. The experiments are performed for $Re = 2640,\ 5280$ and $10\,700$. Using Fourier-based proper orthogonal decomposition (POD), the dominant modes that describe the velocity and vorticity fields are extracted. We employ a new method of averaging POD modes from different experimental runs using a phase-synchronisation with respect to a common basis. For the dominant azimuthal wavenumber $m = 1$, the first and second POD modes of the axial velocity have opposite signs and appear as embracing helical structures, with opposite twist, while, for the same parameters, POD modes of the radial velocity extend to the axis of symmetry and, interestingly, also show a helical shape. The $(m = 1)$-POD modes for the azimuthal vorticity appear as two separate structures, consisting of C-shaped loops in the region away from the axis and helically twisted axial tubes close to the axis. The corresponding axial vorticity modes are cone-like and appear as inclined streaks of alternate sign in the r–z-plane, similar to velocity streaks seen in wall-bounded shear flows. Temporal analysis of the dynamics shows that a $(m = 1)$ two-mode velocity POD representation precesses with a Strouhal number of approximately $St = 0.05$, while the same reconstruction based on vorticity POD modes has a slightly higher Strouhal number of $St = 0.06$.

Key words: jets, low-dimensional models

1. Introduction

The high-Reynolds-number round jet is one of the canonical configurations for investigations into the emergence and dynamics of turbulent coherent structures. It has been extensively studied both from the perspective of fundamental turbulence physics, as well as engineering applications. The basic self-similar statistical structure has been theoretically established, as to the first-order (mean) and second-order (root mean square, r.m.s.) statistical moment profiles (Pope 2000), while the coherent structures are still actively pursued.

Turbulent jets occur in many natural phenomena, from geysers to volcanoes, and in numerous engineering devices, from jet engines to hair blowers. The coherent structures within such jets are important for the mixing and transport of scalars and momentum, and their motion can also be used to estimate volume flow rates, for example, in tracking the amount of spillage from a gushing jet at the ocean's bottom following the Deepwater Horizon disaster (McNutt *et al.* 2012). Philip & Marusic (2012) show that these coherent structures play an important role in mixing and entrainment in turbulent jets and wakes.

Experimental quantitative studies have been limited by the available technologies of the day, from flow visualisation, single hot-wires to rakes of hot-wires, to planar particle image velocimetry (PIV), then stereo-PIV and, most recently, the emergence of tomographic PIV (Tomo-PIV) over the past two decades, where measurement of three-dimensional velocity fields has become feasible (Elsinga *et al.* 2006, 2008; Schröder *et al.* 2008; Westerweel, Elsinga & Adrian 2013). In this work, we focus on extracting the dominant modes that most suitably describe a turbulent jet from volumetric measurements. The study of modes can shed light on the turbulent dynamics of organised fluid elements, which subsequently can be used to develop reduced-order models of the jet and, for example, design a control strategy to diminish undesired jet noise (Jordan & Colonius 2013).

Numerous modal analysis techniques have been proposed, with the most popular and widespread ones in the fluid dynamics community being proper orthogonal decomposition (POD) (Lumley 1967, 1970), dynamic mode decomposition (DMD) (Schmid 2010, 2022), Spectral proper orthogonal decomposition (SPOD) (Towne, Schmidt & Colonius 2018; Schmidt *et al.* 2018), and the resolvent analysis (McKeon & Sharma 2010). In light of recent advances in machine learning (ML) techniques, this new methodology has also been blended with conventional modal analysis methods and extended to data-driven models (Otto & Rowley 2019; Duraisamy, Iaccarino & Xiao 2019). Taira *et al.* (2017) reviewed different techniques used in the turbulence community with a description of the methods and an inclusion of implementation examples. In their subsequent paper (Taira *et al.* 2020), they present an outlook on how modal analysis results can be interpreted for different flow conditions, both in fundamental turbulence research and in engineering applications.

The POD method is the earliest modal analysis method used to objectively extract a hierarchy of coherent structures for turbulent flows. It decomposes the turbulence signal into a set of orthogonal basis functions, referred to as the proper orthogonal modes, ranked by the variance they contain, as measured in a defined norm such as, e.g. kinetic energy or enstrophy. The first few POD modes will thus represent the essential large-scale coherent structures that capture the essential variance of the turbulent flow. If the flow geometry allows the exploitation of a symmetry or periodicity in a particular coordinate direction, the POD modes in this direction degenerate into Fourier modes (see Lumley 1967), resulting a composite Fourier–POD analysis of the flow-field sequence. For the round jet of our configuration, the azimuthal direction presents a statistical axisymmetry. Hence, we choose to use the POD analysis in the non-homogeneous radial and axial coordinate directions, while employing a Fourier transform in the periodic azimuthal direction.

The present configuration represents a fully developed turbulent flow issuing from a circular pipe, flush with the bottom of the tank. The range of length and time scales, as well as the time resolution of the volumetric data, are limited by both the employed imaging method and the finite image memory of the cameras. These limitations determine the total number of volumes in each experimental run, which in turn governs the convergence of the POD estimates.

In table 1, we summarise, in chronological order, the most relevant investigations on coherent structures and dominant modes for the round jet. Understanding coherent structures in a jet has seen more focus on the near-field than the far self-similar region (Yoda, Hesselink & Mungal 1994). It has long been known from flow-visualisation experiments that the near-field consists of Kelvin–Helmholtz instability-driven axisymmetric vortex rings (Crow & Champagne 1971). However, the existence of large-scale structures beyond the potential core was not as evident as it was for the near-field. Two-dimensional images of the jet in the far-field obtained by laser-induced fluorescence experiments by Dimotakis, Miake-Lye & Papantoniou (1983) showed the outline of the jet either as a zig–zag (antisymmetric) or symmetric pattern. Based on this observation, they proposed that an expanding spiral mode describes the far-field structures. However, this was challenged based on subsequent measurements: it was in fact the helical modes that dominated this region (Tso & Hussain 1989; Yoda *et al.* 1994). Fourier-based POD analysis of hot-wire rakes data has also shown that the lower axisymmetric mode $m = 0$ dominates in the near-field, while higher modes prevail in regions far from the nozzle (Glauser *et al.* 1987; Jung, Gamard & George 2004; Iqbal & Thomas 2007; Tinney *et al.* 2008*a*). Time integration of the two-dimensional rake data, assuming a convection velocity, have been used to visualise three-dimensional structures. Iqbal & Thomas (2007) used the λ_2-criterion, rendered non-dimensional by the approximate constant convective velocity and the nozzle radius. They showed that lower-order structures at $z/D = 3$ consisted of toroidal shear layer vortices, while the higher azimuthal modes were characterised by streamwise 'vortical braids', reminiscent of a mixing layer. Further downstream, at $z/D = 6$, helical vortical structures about the streamwise direction appear, with no preferred orientation. These helical structures dominate further downstream, up to the end of the measurement region. Using a similar approach, Tinney *et al.* (2008*b*) observed organised jet columns with a distinct azimuthal structure; however, the vortical structures become more disorganised further downstream, at $z/D = 7$. Recently, modal analysis of DNS data by Mullyadzhanov *et al.* (2018) demonstrated that the most important $m = 1$ azimuthal mode resulted in helical POD modes. The first two POD modes appeared as mirror modes, with similar shapes but different helical orientation.

In addition to POD, coherent structures from instantaneous flow fields have been presented based on simulations and volumetric measurements. The organised axisymmetric vortical structures, caused by a Kelvin–Helmholtz instability in the near-field, breaks down into disorganised azimuthal structures in the far-field. Suto *et al.* (2004) proposed a conceptual model of horseshoe-like eddies, with legs inclined downstream, based on their simulation and experimental study of a jet. The proposed eddies were geometrically similar to the horseshoe/hair-pin eddies extensively researched in wall-bounded turbulence (Head & Bandyopadhyay (1981), Marusic (2001), Ganapathisubramani *et al.* (2005)).

Extraction of POD modes in jets, using a rake of hot-wire measurements, has been reported in the literature, starting from Glauser *et al.* (1987), wherein the authors used seven single hot-wires placed along the radial direction, thus measuring only the streamwise velocity component. Extending this to a rake of 138 hot-wires, Citriniti & George (2000) measured the streamwise velocity in a two-dimensional cross-sectional

Authors	Re_D	Investigation method (Velocity components Measured)	Region (z/D)	Analysis
Dimotakis *et al.* (1983)	2500	LIF	0−35	Coherent Structures
Glauser *et al.* (1987)	110 000	7 single wires Hot-wire sensors (U_z)	3	POD
Yoda *et al.* (1994)	1000−4000	Scanning LIF	30−83	Coherent Structures
Citriniti & George (2000)	80 000	Rake of 138 single wires Hot-wire sensors (U_z)	3	Fourier POD
Jung *et al.* (2004)	78 400−156 800	Rake of 138 single wires Hot-wire sensors (U_z)	2−6	Fourier POD
Gamard *et al.* (2004)	40 000−84 700	Rake of 139 single wires Hot-wire sensors (U_z)	15−69	Fourier POD
Matsuda & Sakakibara (2005)	1500−5000	Stereoscopic PIV (2D−3C)	20−50	Conditional Averaging
Iqbal & Thomas (2007)	380 000	Twin rake of 14 X-wires Probes (3C)	3−12	Fourier POD
Tinney *et al.* (2008*a*,*b*)	1×10^6	Stereoscopic PIV (2D−3C)	3−8	Fourier POD
Schmid *et al.* (2012)	5000	Tomographic PIV (3D−3C)	Up to 13	DMD
Casey *et al.* (2013)	2640−10 700	Scanning tomographic PIV (3D−3C)	45−55	Tracking Structures
Violato & Scarano (2013)	5000	Tomographic PIV (3D−3C)	Up to 10	POD
Mullyadzhanov *et al.* (2018) (Jet with co-flow)	5290	DNS	2.5−40	Fourier POD
Ianiro *et al.* (2018) (Swirling jets)	1000	Tomographic PIV (3D−3C)	Up to 5	DMD
Samie *et al.* (2022)	7300	DNS	Up to 30	Conditional Averaging

Table 1. Summary of important studies on coherent structure analysis in turbulent round jets using modal decomposition methods, coherent structure identification and conditional averaging methods. This list focuses primarily on experimental studies, but also comprises the latest relevant direct numerical simulations. The velocity components measured in the experimental studies is indicated as well. The symbols/abbreviations are as follows: U_z denotes the axial velocity, 3C stands for 'three components', 2D-3C represents 'three components' in a plane and 3D-3C indicates 'three components in a volume'.

plane (r–θ-plane) in the near-field at $z/D = 3$, which was then used to analyse POD modes, while a Fourier decomposition is performed in both the azimuthal and time coordinates. Using the same hot-wire arrangement, their analysis was extended to modes in a wider range of streamwise planes: in the near-field ($z/D = 2$ to 6) by Jung *et al.* (2004) and in the far-field ($z/D = 20$ to 69) by Gamard, Jung & George (2004). These studies reported that the dominant azimuthal mode is $m = 0$ near the jet, while $m = 2$ prevails for $z/D > 6$.

Iqbal & Thomas (2007) presented POD results based on three velocity components, measured using a rake of 14 $\times$-wire probes arranged in two perpendicular radial lines in the near-field (covering the interval $3 \leqslant z/D \leqslant 12$) of a turbulent jet. The X-wires measure

two velocity components at a time, but need to be rotated to measure the remaining third, thus excluding simultaneous measurements of all three components, as is feasible using Tomo-PIV. The authors note that $m = 2$ dominates for the streamwise component, while the $m = 1$ azimuthal mode prevails over other modes in the near-field, but its dominance diminishes further downstream. In the same study, the Strouhal number, where the eigenvalue spectra peaks for the different azimuthal modes, is reported: based on the local momentum thickness and the centreline velocity, it scaled linearly with the azimuthal mode number.

Tinney *et al.* (2008*a*) performed a POD analysis on Stereo-PIV measurements in a cross-sectional plane in the near-field of a jet issuing from a converging nozzle of diameter 50.8 mm into an anechoic chamber at a Mach number of 0.85. They looked at the modal energy distribution for each component of velocity in the near-field of the jet, and concluded that lower-order azimuthal modes dominate in the potential core and the high-speed side of the shear layer, i.e. $r < r_{0.5}$, while higher-order modes have been found on the outer low-speed side. Here, $r_{0.5}$ is referred to as the half-radius, where the mean velocity is half the centreline value. In terms of velocity components, lower-order modes are dominated by the axial velocity far more than the other two components, which contribute more to higher-order structures.

Violato & Scarano (2013) used time-resolved Tomo-PIV measurements in the near-field (up to $10D$) of a turbulent water jet at $Re = 5000$, and analysed the relation between coherent structures and sound production. They performed POD analysis of the velocity, vorticity, Lamb vector and its second derivative obtained using the Tomo-PIV technique. The primary pair of velocity and azimuthal vorticity modes represented the travelling toroidal vortices after pairing with a characteristic Strouhal number of $St = 0.36$. The secondary travelling velocity pair exhibited helical motion.

A brief historical perspective of Fourier-based POD modes is included in the recent work by Hodžić *et al.* (2024). Mullyadzhanov *et al.* (2018) performed a POD analysis on the direct numerical simulation of a jet from a fully developed turbulent pipe introduced into the computational domain together with a co-flow chosen as 0.27 times the jet velocity. They analysed the flow field by dividing the domain into five sub-domains extending from $z/D = 2.5$ to 40, with different radii. By performing a Fourier decomposition of the velocity fields in the azimuthal direction, they focused on the POD modes in the far-field region. The dispersion relations between the frequency and the phase velocity has been reported for the first five azimuthal modes. A similar analysis based on large-eddy simulation (LES) of a jet in a cross-flow has been presented by Mullyadzhanov, Abdurakipov & Hanjalić (2017).

Following the proposition of horseshoe vortices, there have also been studies based on analysing instantaneous coherent structures. Matsuda & Sakakibara (2005) used time-resolved stereo-PIV to analyse a turbulent jet, using Taylor's hypothesis for the streamwise direction. They assumed a constant convection velocity to construct the three-dimensional coherent structures from the planar measurements and observed horseshoe vortices around the shear region, by plotting iso-surfaces of λ_2-structures. By conditional averaging, they also reported horseshoe structures at 1.5 times the half-radius. Hori & Sakakibara (2004) previously used scanning stereo-PIV techniques to obtain volumetric three-dimensional velocity fields and visualised vortical structures in the shear layer. Schmid, Violato & Scarano (2012) performed time-resolved Tomo-PIV measurements in the near-field of a transitional jet at $Re = 5000$. In this study, the authors combined volumetric velocity measurements with DMD analysis to extract coherent flow structures. The analysis revealed two dominant modes with frequencies corresponding to $St = 0.325$ and $St = 0.646$.

Both dynamic modes, visualised by λ_2-criterion, showed axisymmetric vortex rings, with the second mode being more concentrated near the nozzle, signifying a primary instability.

Casey *et al.* (2013) measured the time-resolved velocity field in the far-field ($z/D = 45$ to 55) of a fully turbulent round jet using a scanning Tomo-PIV technique. The method enabled them to obtain volumetric velocity fields over a substantial depth, compared with the Tomo-PIV technique. Coherent structures have been visualised for three different Reynolds numbers in the range $Re = 2640$ to 10 700, using a vorticity magnitude criterion. The coherent structures showed a collection of C-shaped structures convected streamwise at low Reynolds numbers and long tube-like structures at high values of Re. This study further looked at the temporal evolution of several tube-like structures and quantified the streamwise variation of structural characteristics, such as the radial position, orientation, turbulence production and dissipation, and the vortex deformation.

Ianiro *et al.* (2018) used a three-camera Tomo-PIV set-up to study the vortical structures in the near-field of a transitional swirling jet (up to $z/D = 5$), at a Reynolds number of $Re = 1000$ for swirl numbers in the range of 0 to 0.8. The coherent structures, extracted using DMD, showed helical vortices in the near-field, with pairing of three vortices in the shear layer. The authors state that the precessing vortex core interacts with the helical vortices, enhancing both the breakdown and precession, and supresses the vortex pairing. Recently, Samie *et al.* (2022) analysed coherent structures in the near- and intermediate-fields up to $z/D = 25$, based on the direct numerical simulation (DNS) of a turbulent jet, at $Re = 7300$. Using conditional averaging, they identified both symmetric and asymmetric horseshoe vortices similar to those seen in wall-bounded flows. The near-field consists of horseshoe vortices which tend to group together, forming spiral and streamwise-aligned large-scale structures in the intermediate field. The authors further observe very-large-scale motions in the intermediate field of the jet.

From the comprehensive review of the literature, we see that most three-dimensional modal POD analyses of jets have been performed with data from DNS. Analyses based on physical measurements, however, have been limited to cross-sectional planes, either using hot-wire rakes or stereo-PIV techniques. The extracted structures are then visualised in the axial direction using Taylor's hypothesis of frozen turbulence. In this present work, we perform a Fourier-based POD analysis of time-resolved three-dimensional volumetric velocity and vorticity fields measured in the far-field of the jet using a scanning Tomo-PIV technique, introduced by Casey *et al.* (2013). In an attempt to attain a long time-series of snapshots, which is imperative for a proper convergence of the statistics, such volumetric image-based techniques are limited by the memory of the camera. For this reason, we present results (dominant POD modes) by averaging over many experimental runs, which not only ensures improved convergence, but also accounts for variations in the experimental conditions. Our analysis is then extended to the vorticity field. For both the velocity and vorticity fields, the dominant modes and their dynamics are extracted and discussed.

2. Experimental set-up and methodology

2.1. *Turbulent jet*

Figure 1 presents a schematic of the experimental set-up, showing the laser illumination and the four-camera imaging system. The water-tank test section consists of a 500 mm high octagonal acrylic tank with each side measuring 185 mm. The jet enters the tank from a bottom mounted nozzle of inner diameter $D = 5$ mm. The ratio of the confinement cross-section to the nozzle cross-section is 8.4×10^3. Violato & Scarano (2013) in their Tomo-PIV experiments used a similar octagonal tank with a confinement ratio of 3.8×10^3. Water from a constant small-head tank flows through a 500 mm long straight

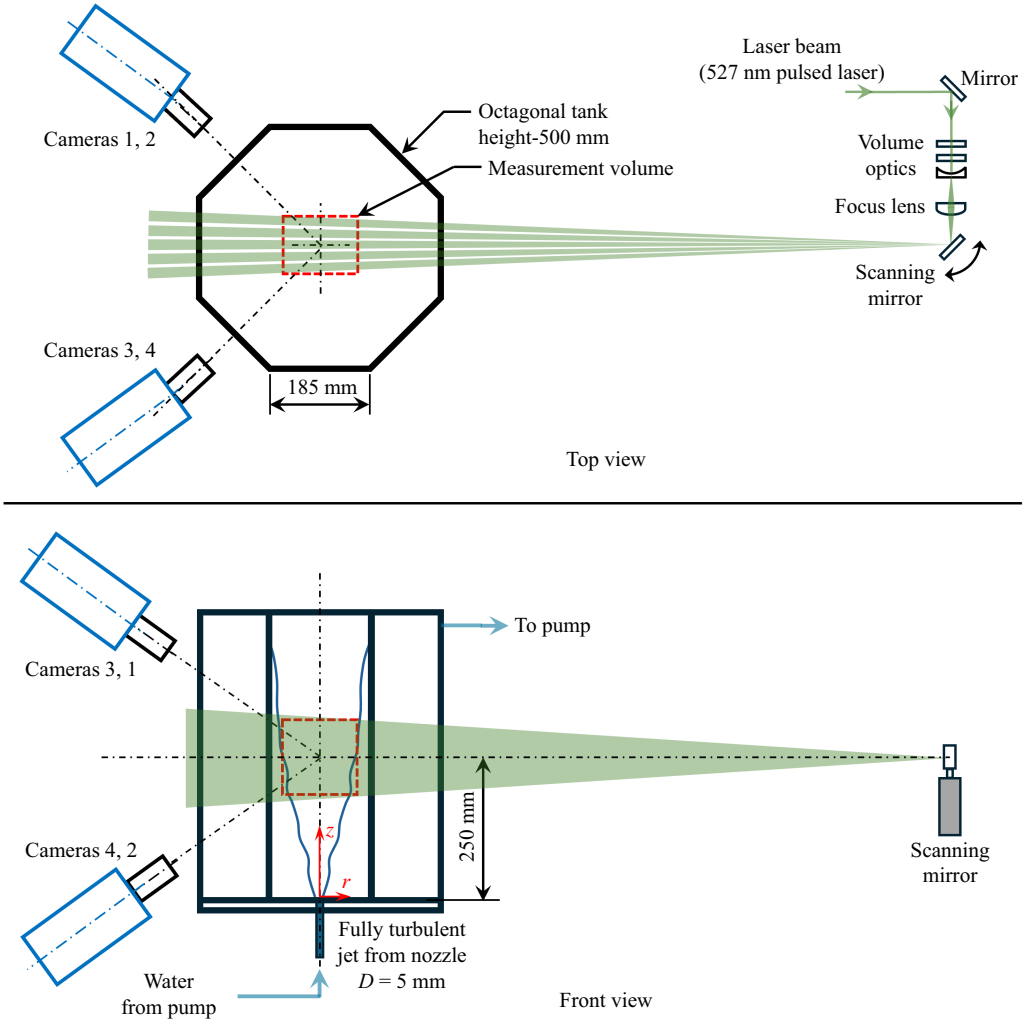

Figure 1. Schematic top and front views of the experimental water tank, along with the illumination and the imaging system. The five-volume scan used with the Fast-scan and Triple-pulse scanning protocols is illustrated in the figure. The bounding volume of the scanning is represented by the red-dashed lines, with the total size depending on the scanning protocol. It measures approximately 130 mm $\times$ 130 mm in the $r-z$-plane and 100 mm in the scanning direction. Appendix contains a photograph of the camera arrangement.

steel-pipe before entering the test section. This ensures fully developed turbulent flow conditions at the outlet of the nozzle into the flat bottom of the tank. A constant flow rate through the nozzle is achieved by adjusting the height of the overhead tank and the rotation speed of a displacement pump feeding water into it. The water level in the octagonal tank is maintained at a constant height using overflow lines, with three outlets equally spaced around the periphery. The flow rate is set to 0.63, 1.26 and 2.52 litres per minute. The corresponding Reynolds numbers, $Re = \rho V_j D/\mu$, are 2640, 5280 and 10 700, where V_j is the average exit velocity of the jet at the nozzle. The experimental conditions corresponding to these three Reynolds numbers are labelled as $Re2$K, $Re5$K and $Re10$K; the governing parameters for these three cases are summarised in table 2. We compute the dissipation rate considering all twelve derivative correlations of velocity fluctuations as $\langle 2\nu s_{ij} s_{ij} \rangle$, where $s_{ij} = (1/2)(\partial_j u_i + \partial_i u_j)$. The Kolmogorov scale at the

Conditions	*Re*2K	*Re*5K	*Re*10K
Re	2640	5280	10 700
V_j (m s^{-1})	0.53	1.06	2.15
η (mm)	0.310	0.210	0.140
η_c (mm)	0.204	0.138	0.092
τ_c (ms)	41.5	19.0	8.5
Scanning protocol	Triple pulse	Fast scan	Double pulse
Image acquisition rate (fps)	260	1279	450
$\delta t/\tau_c$	0.20	0.25	0.26
No. of sub-volumes	5	5	9
$L1 \times L2 \times L3$ (mm^3)	133 × 128 × 83	99 × 99 × 72	133 × 129 × 91
δ_I/η_c	16	24	30
δ/η_c	4.1	6.0	7.5
Δt (ms) [$\Delta t/\tau_c$]	57.7 [1.40]	4.7 [0.25]	40.0 [4.70]
Time-series length, N (volumes)	209	524	174
Experimental runs	10	10	15
Size of polar grid $\mathbb{P}$ ($R \times H$) (mm^2)	35 × 128	30 × 99	40 × 129

Table 2. Experimental conditions and important turbulent parameters for the three Reynolds numbers cases and the Tomo-PIV algorithm. Here, V_j is the mean velocity at the nozzle exit and η is the Kolmogorov scale computed as $(\nu^3/\varepsilon)^{1/4}$, with ν as the kinematic viscosity and ε as the dissipation rate. The dissipation rate is computed as $\langle 2\nu s_{ij}s_{ij}\rangle$, where $s_{ij} = (1/2)(\partial_j u_i + \partial_i u_j)$ at $z = 250$ mm. η_c is the Kolmogorov scale after correction by a factor $f_\eta \approx 1.5$, which is based on η_{mag} computed using high-magnification experiments. $\tau_c = (\nu/\varepsilon_c)^{1/2}$ is the Kolmogorov time scale based on the corrected dissipation. The complete measurement volume is made up of many sub-volumes determined by the number of steps used in the scanning protocol. $L1 \times L2 \times L3$ denotes the size of the velocity grid with a grid data spacing $\delta = \delta_I/4$, where δ_I is the size of the interrogation window. The time step used for velocity calculations is represented by δt and the time step between two consecutive velocity volumes is referred to by Δt. The variables R and H are respectively the radius and height of the cylindrical volume grid onto which the field is interpolated.

middle of the measurement region, averaged over many realisations, is approximately 0.3, 0.2 and 0.14 mm for *Re*2K, *Re*5K and *Re*10K, respectively. For better estimates of η, these computations are performed using high-magnification measurements at $Re = 10\,700$, with an optical magnification of 2.25× (referred to as *Re*10KZ). Five runs have been performed with a smaller measurement volume of $56 \times 46 \times 20$ mm^3. At $z = 250$ mm, we obtain $\eta_{mag} = 0.092$ mm, a value approximately 1.5 times smaller than the base magnification case. The axial variation of η for all three Reynolds numbers and a comparison with the high-magnification case are shown in figure 23. The Kolmogorov scale based on the self-similar, normalised dissipation rate $\hat{\varepsilon} = \varepsilon r_{1/2}/\langle Uzc\rangle^3 = 0.017$ from measurements of Panchapakesan & Lumley (1993) (PL93), at $z = 250$ mm are 0.280, 0.156 and 0.093 mm for *Re*2K, *Re*5K and *Re*10K, respectively. They obtained ε from the balance of the kinetic energy budget and compared these values with estimates based on direct measurements of derivatives, similar to our approach. Hussein & George (1990) estimated $\hat{\varepsilon} = 0.0262$, 0.028 for axisymmetry and isotropic assumptions, respectively. The corresponding values of η for *Re*10K are 0.084 and 0.082 mm. It is interesting to note that η in the current high-magnification experiments is close to previous estimates. Hence, we use the factor, $f_\eta = \eta/\eta_{mag} = 1.52$, to correct the Kolmogorov scale η_c for the other two Reynolds numbers. The density and dynamic viscosity of water are $\rho = 998$ kg m^{-3} and $\mu = 1.0\times10^{-3}$ Pa s. Between 10 and 15 experimental runs were conducted for each flow rate to obtain an adequate convergence of the statistics.

2.2. *Velocity measurements*

We use the commercial LaVision tomographic PIV system for image acquisition. The illumination system consists of a high-speed 527 nm Nd-YLF dual-cavity pulsed laser (Litron LDY300 PIV). The beams from the laser heads are combined and directed by mirrors to pass through a set of volume optics which expand the beams slowly in both directions to create a laser slice. These optics change the cross-section of the beam from an ellipse to a rectangle. The rectangular expanding beam is then focused on a scanning mirror attached to a galvanometer, which can rotate horizontally in precise steps about its vertical axis. Hence, the step-wise rotation of the galvanometer causes the pulsed laser slices to span the measurement volume centred in the jet's far-field at $z/D = 50$. Each slice is approximately 25 mm wide, and, using a slight overlap, the final volume spans approximately 100 mm. Figure 1 shows the case where each rotation cycle consists of five steps and thereby creates five sub-volumes within the total measurement region. Note that only one sub-volume is illuminated at any given time. The galvanometer's rotation is precisely controlled by a signal generator using three different protocols: triple pulse (TP), fast scan (FS) and double pulse (DP). The different protocols are based on the number of laser pulses flashed in each step. One, two or three pulses are flashed per step of the scanning mirror in the FS, DP and TP protocols, respectively. The scanning signal consists of 5, 5 and 9 steps for FS, DP and TP. This forms either 5 or 9 planes in the depth direction with a volume thickness of 25 or 17 mm each. The cameras and the laser are synchronised such that the frequency of the laser flashes ($1/\delta t$) is matched to the image acquisition frequency, so that every laser flash is recorded in one frame. Hence, FS, DP and TP protocols will have one, two and three frame(s) recorded in each sub-volume. Each volume corresponding to the complete sweep of the mirror will consist of 6, 18 and 15 laser flashes or frames for FS, DP and TP protocols. The timing details of the galvanometer and the camera frame with timing charts can be found from Casey *et al.* (2013). Due to different image acquisition rates, pulse protocols and number of sub-volumes, the total length of the time series varies between the three Reynolds numbers. We thereby get 209, 524 and 174 volumes for *Re*2K, *Re*5K and *Re*10K, which are separated by different flow times Δt.

We use four 2016×2016 pixel CMOS high-speed cameras (PCO, Dimax) for image acquisition. The maximum acquisition rate is 1279 frames per second (fps) at full resolution, and the cameras can store 3153 images in its built-in memory and has a pixel size of 11 μm. The arrangement of the cameras is shown in figure 1 and in a photo in figure 20 in Appendix A. Cameras 1 and 3 look down on, and cameras 2 and 4 look up at the measurement region, making their effective overlap ellipsoidal. Each camera looks through a water-filled angled prism to minimise optical distortions. The cameras form an angle of approximately 30° with respect to a horizontal plane passing through the measurement volume centre. Identical lenses with an aperture $f/32$ are used with Scheimpflug attachments to ensure sufficient depth of focus for the full scanned volume. The calibration process establishes the spatial relation between the physical coordinates in the measurement region and the image coordinates. The optical system has a nominal image magnification of $M = 0.16$ and the diffraction-limited spot size is calculated to be 48 μm (approximately 4 pixels). This is performed using 11 planes by traversing a dual-plane, double-sided calibration plate (Type 22 from LaVision) over a depth of 90 mm. Subsequently, the volume self-calibration step (introduced by Wieneke 2008) is performed using the 10 000 brightest reconstructed particles to push the error in the calibration to levels below 0.1 to 0.2 pixels. This step corrects for any changes to the optical set-up during the experiments. For seeding, we use 20 to 50 μm PMMA-encapsulated Rhodamine-B fluorescent particles, which are slightly heavier than water. More details of

the scanning protocols and the experiments can be found from Casey *et al.* (2013). The particle concentration lies in the range of 0.015−0.025 particles-per-pixel with a source density of 0.1−0.3.

2.3. *Tomographic reconstruction and velocity deduction*

We use the Tomo-PIV correlation method to deduce velocities from the particle images, which is performed in two main steps in DaVis 8.2 from LaVision. In the first step, the three-dimensional voxel intensities at the particle locations are reconstructed using the images from the four cameras to form a volume of intensities for each time step. Following this step, a correlation of reconstructed particles over two subsequent times is determined to obtain the corresponding three-dimensional velocity field. Even though the illuminated volume is a cuboid, velocity vectors are restricted to an ellipsoidal region contained within the cuboid due to the overlap in the angled views of all the cameras. Thus, all 5 or 9 sub-volumes do not contain the same number of reconstructed particles. As a consequence, our analysis is mostly restricted to only the central three of the five sub-volumes, where the particle density and reconstruction intensities are sufficiently high. The acquired raw particle images are preprocessed to normalise the particle intensities and to remove any constant background. The reconstruction of each sub-volume is performed separately using the corresponding self-calibration that is obtained with particles from the same sub-volume. The MART algorithm built into the DaVis software is employed for this step, forming a stack of planar intensity sections. To remove the ghost intensities, reconstruction in each sub-volume is performed over a depth greater than the illumination depth. Reconstruction in depth, where the signal-to-noise ratio (SNR) ≥ 2.5, is only considered for subsequent steps. The reconstructed intensity-planes in these sub-volumes are then 'stitched' together, using in-house MATLAB routines, to form the total volume, which now counts up to 1500 planes in depth. Note that there is a small time lag between each sub-volume within this total volume. The direct correlation method is used for the three-dimensional velocity eduction. The correlation is performed iteratively in three to four steps by reducing the interrogation window size from $128 \times 128 \times 128$ to $48 \times 48 \times 48$, with a constant overlap of 75 %. For the *Re*10K case, which uses nine planes, velocities are deduced with a final interrogation window size of $40 \times 40 \times 40$ and 75 % overlap. This set-up yields instantaneous velocities (U, V, W) on a Cartesian grid with a uniform grid spacing $\delta = \delta_I/4$ (see table 2), where δ_I is the interrogation window size. The instantaneous vorticity field $(\widetilde{\omega_x}, \widetilde{\omega_y}, \widetilde{\omega_z})$ is then calculated using fourth-order finite-difference schemes. The accuracy of the resulting velocity and its gradients is quantified by calculating the residual in the continuity equation. One approach consists of obtaining the correlation coefficient of the terms of the continuity equation, $\Delta U/\Delta x$ and $-(\Delta V/\Delta y + \Delta W/\Delta z)$. These terms are calculated over cuboidal volumes with size $W_{CV} = \delta_I$. The correlation coefficient computed with volumes of size W_{CV}, $2W_{CV}$ and $4W_{CV}$ for *Re*10K are 0.79, 0.91 and 0.96, respectively. The values are comparable to 0.82 in stereo measurements following Ganapathisubramani, Lakshminarasimhan & Clemens (2007). The accuracy has been reported in great detail by Casey *et al.* (2013).

For the Fourier analysis in the current study, we require the Cartesian velocity and vorticity on a Cartesian grid $\mathbb{C}$ to be mapped onto a cylindrical grid $\mathbb{P}$, centred on the jet axis. For this, we first determine the axis of symmetry of the jet by tracing the vertical locus of the maximum mean axial velocity over many acquired realisations. The Cartesian velocity components (U, V, W) are then transformed to polar velocity components (U_r, U_θ, U_z) with respect to our identified axis. Similarly, the vorticity components $(\widetilde{\omega_x}, \widetilde{\omega_y}, \widetilde{\omega_z})$, from the Cartesian grid, are transformed to their corresponding

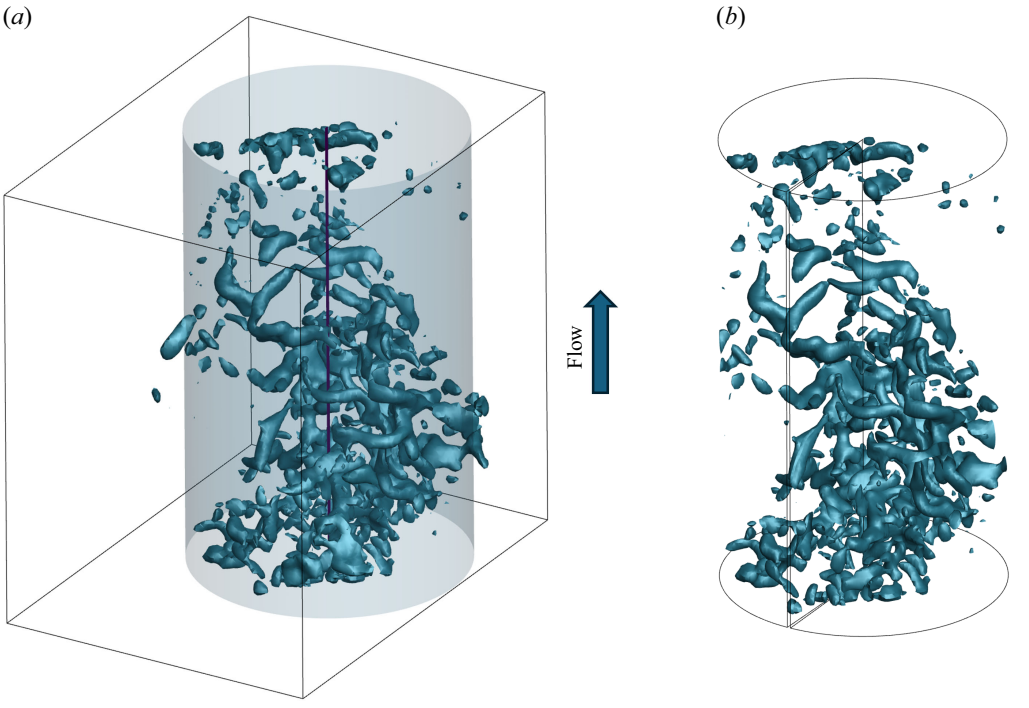

Figure 2. Coherent structures visualised using iso-surfaces of vorticity magnitude $|\widetilde{\boldsymbol{\omega}}| = 32$ (s^{-1}) in (a) the actual Cartesian grid $\mathbb{C}$ and (b) the interpolated polar grid $\mathbb{P}$ for the case R5K. The rectangular domain in panel (a) measures $99 \times 99 \times 72$ mm^3, from which a cylindrical domain of radius $R = 30$ mm and height $H = 99$ mm, indicated by the blue cylindrical surface, is extracted. The purple vertical line in panel (a) indicates the jet axis used for our coordinate transformation. Note that the Cartesian components in $\mathbb{C}$ are first transformed to polar components in $\mathbb{C}$ and then interpolated onto $\mathbb{P}$.

polar components ($\widetilde{\omega_r}$, $\widetilde{\omega_\theta}$, $\widetilde{\omega_z}$). The polar component values on the Cartesian grid are then interpolated onto the $\mathbb{P}$ grid from their values on the $\mathbb{C}$ grid using a cubic interpolation implemented in the *griddata* function (MATLAB). Figure 2 shows the actual coherent structures on the $\mathbb{C}$ grid and after interpolation onto the cylindrical $\mathbb{P}$ grid. The grid spacing of the polar grid $\mathbb{P}$ shown in figure 2(b) is $\Delta r = 0.5$ mm, $\Delta\theta = 2\pi/256$ and $\Delta z = \delta$, where δ is the original Cartesian axial spacing. The radius R and height H of the cylindrical volume grid, used for analysing the different Reynolds number cases, are summarised in table 2.

2.4. *Fourier-based proper orthogonal decomposition (POD)*

We use the Fourier-based POD to identify and extract the dominant coherent structures that describe the jet.

Due to the axisymmetry of the jet, the velocity field in the azimuthal direction is statistically homogeneous. Consequently, a Fourier decomposition in this direction naturally provides the relevant eigenfunctions, eliminating the need for POD (Lumley 1967). However, the radial and streamwise directions are inhomogeneous, requiring POD to extract coherent structures in these directions. This allows us to analyse each azimuthal Fourier mode independently, significantly reducing the size of the data matrix for the overall decomposition.

A similar analysis has recently been performed, using direct numerical simulation data, by Mullyadzhanov *et al.* (2018), where POD of a few azimuthal Fourier modes was used to describe a turbulent jet.

In what follows, we will use the following nomenclature: the instantaneous radial velocity, denoted by $U_r = \langle U_r \rangle + u_r$, and the instantaneous azimuthal vorticity, represented by $\widetilde{\omega_\theta} = \langle \widetilde{\omega_\theta} \rangle + \omega_\theta$. Here, the angled brackets $\langle \cdot \rangle$ indicate the mean-flow (averaging) operator and the lower case symbols represent fluctuating components.

We perform the Fourier decomposition of both the measured fluctuating velocity and the fluctuating vorticity fields. However, the mathematical formulation is described later only for fluctuating velocity, as it remains the same for other quantities. The Fourier decomposition of the fluctuating velocity field, $\boldsymbol{u} = (u_r, u_\theta, u_z)$, results in a set of complex vector fields in Fourier space. We have

$$\boldsymbol{f^m}(r, m, z, t) = (f^m_{u_r}, f^m_{u_\theta}, f^m_{u_z}) = \frac{1}{2\pi} \int_0^{2\pi} \boldsymbol{u}(r, \theta, z, t) e^{im\theta} \, \mathrm{d}\theta, \tag{2.1}$$

where $\boldsymbol{f}$ is the fluctuating velocity field in Fourier space and m stands for the azimuthal Fourier wave number. The cylindrical grid has a uniform azimuthal step size of $2\pi/256$ and hence, we have the wavenumber m varying from 0 to 255. We then apply the triple decomposition of the snapshot data matrix, $\mathcal{D}$, which is constructed with all the components of the fluctuating field $\boldsymbol{f}$. This factorisation decomposes the data series into essential structures, their dynamics and the associated energy, and has become a common method to extract the coherent dynamic processes from snapshot sequences, as reported by Schmid (2022). Note that the fluctuating field, $\boldsymbol{f^m}$, for a given mode m, is only a function of (r, z) and hence yields a compact matrix $\mathcal{D}$. To account for the radial location of the data point in the uneven grid, the velocity at a particular point is weighted by the corresponding volume surrounding it, as $\sqrt{\Delta V} = \sqrt{r \Delta r \Delta z}$. The data matrix is constructed with all three components such that each column corresponds to a snapshot in time. An example of constructing the data matrix is given in Appendix B.

The matrix $\mathcal{D}^m$, for a given Fourier mode m, is expressed as a triple product using the singular value decomposition, as given by

$$\mathcal{D}^m = \mathcal{U}^m \Sigma^m (\mathcal{V}^m)^H, \tag{2.2}$$

where the unitary matrix $\mathcal{U}^m$ contains the spatial modes, the diagonal matrix Σ^m gives the singular values, $(\mathcal{V}^m)^H$ is a unitary matrix and contains the dynamic information of the spatial structures, and the superscript ^{H} represents the Hermitian (conjugate transpose) operation. We use the *svd* function in MATLAB for the above-mentioned factorisation and save the N spatial POD modes. The fluctuating velocity $\boldsymbol{f}^m$ at any given instant t_i can be obtained by summing over all N POD modes according to

$$\boldsymbol{f}^m(r, z, t_i) = \frac{1}{r \Delta r \Delta z} \sum_{n=1}^{N} a_n^m(t_i) \sigma_n^m \phi_n^m(r, z), \tag{2.3}$$

where $a_n^m(t_i)$ signify the time coefficients, σ_n^m represent the singular values and ϕ_n^m are the spatial modes corresponding to the nth POD mode.

The product $\mathcal{C}^m = \mathcal{D}^m (\mathcal{D}^m)^H$ produces the velocity correlation matrix, whose eigenvalues obey $\Lambda^m = (\Sigma^m)^2$. The eigenvalue of $\mathcal{C}^m$ represents the fluctuation energy, k^m, contained in Fourier mode m. The eigenvalues of the correlation matrix constructed

with vorticity components represents the associated enstrophy k_ω^m. The energy contribution of the different Fourier modes and the constituent POD modes are discussed in the results section.

3. Results

3.1. *Mean velocity and Reynolds stresses*

Before launching into extracting and identifying coherent structures, we first present some of the important flow statistics for the jet geometry in this section. The measurement domain is centred about the streamwise location $z/D = 50$. This is sufficiently far from the inlet that the mean velocity profile can be expected to be self-similar. This has been verified by Casey *et al.* (2013), by comparing the radial profile of the mean and r.m.s. velocities with earlier hot-wire and stereo-PIV measurements in the literature (Wygnanski & Fiedler 1969; Matsuda & Sakakibara 2005) for the extreme Reynolds numbers – *Re*2K and *Re*10K. In figure 3, we compare the radial profiles of the mean axial velocity, r.m.s. values of the velocity components and the dominant Reynolds stress for *Re*5K with the hot-wire measurements of Wygnanski & Fiedler (1969) (WF69) at $Re = 10^5$ and Panchapakesan & Lumley (1993) (PL93) at $Re = 1.1 \times 10^4$. Panchapakesan & Lumley (1993) used X-wire probes mounted on a moving shuttle in their measurements. They state that the method is more reliable in outer-region measurements as they eliminate errors associated with stationary hot-wires in resolving flow-reversals. The overlap of the mean axial velocity profiles at different z/D in figure 3(*a*) confirms that the current measurement is in the self-similar region. There is a good agreement with the hot-wire measurements in the mean profile, but the r.m.s. values (figure 3*b*–*d*) are lower than the hot-wire measurements similar to the observations made by Casey *et al.* (2013). The decay of the centreline velocity $\langle U_{zc}\rangle$ follows $1/z$ with a decay constant $B_u = 6.01$ and has a spreading rate of $S = 0.097$, which matches the values reported by PL93 ($B_u = 6.06$ and $S = 0.096$). The values of these parameters for *Re*2K and *Re*10K are (5.25, 0.077) and (5.10, 0.105), respectively. The axial variation of the centreline velocity and the jet half-radius for *Re*5K is shown in figure 22. The r.m.s. values are closer to PL93, which has a similar order of magnitude for the Reynolds number. The current measurements also capture the off-axis peak (at $z/D = 55$) of the axial fluctuation, highlighted by Panchapakesan & Lumley (1993). This peak is attributed to the production of kinetic energy which has its maximum around this location. The current measurement of the Reynolds stress $\langle u_r u_z\rangle$ matches well with PL93 up to $r/r_{1/2} \approx 0.5$, but falls below PL93 after that. Lower r.m.s. values and $\langle u_r u_z\rangle$ are primarily due to smoothing inherent in the correlation technique.

Figure 4(*a*) shows the normalised time-averaged mean velocity contour $\langle U_z\rangle/\langle U_{zc}\rangle$ in the r–z-plane, after averaging in the θ-direction, for different Reynolds numbers Re. The coordinates are normalised by the nozzle diameter D. It is clear that the jet width increases with Re. Note that the radial extents of the three cases are not the same due to the different scanning protocols employed. The largest cylindrical measurement domain, for *Re*10K, shows zero-velocity regions in the right corners which fall outside the reconstruction region. These corners are included for completeness of the grid; their inclusion, as we will see, does not affect the dominant POD modes.

The most contributing Reynolds stress, $\langle u_r u_z\rangle$, is presented in figure 4(*b*). Due to the self-similar mean profiles and our normalisation with the local centreline velocity, the peak of $\langle u_r u_z\rangle$ occurs at $r/D \approx 3$ in all cases, which is approximately 70 % of the jet half-radius. The contours of $\langle u_r u_z\rangle$ also show a slight inclination with z which is due to an increase in the jet width.

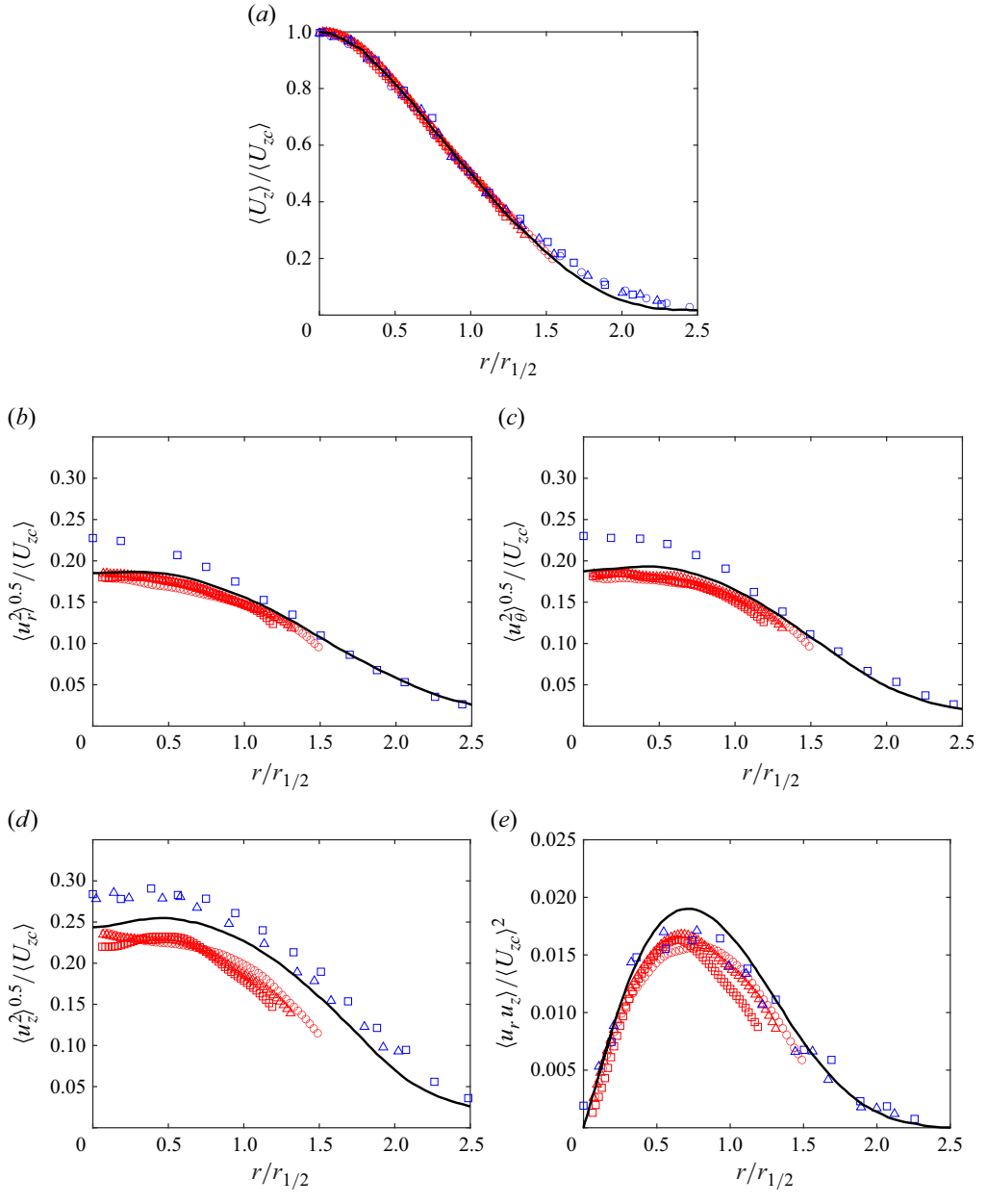

Figure 3. Comparison of the present radial-profile measurements of (*a*) mean axial velocity $\langle U_z \rangle$, (*b*) r.m.s. radial velocity $u_{r,rms}$, (*c*) r.m.s. azimuthal velocity $u_{\theta,rms}$,(*d*) r.m.s. axial velocity $u_{z,rms}$ and (*e*) Reynolds stress $\langle u_r u_z \rangle$ for the *Re*5K case, with hot-wire measurements. For normalisation, the local centreline velocity $\langle U_{zc} \rangle(z)$ is chosen as the velocity scale, and the jet half-radius $r_{1/2}$ is chosen as the length scale. The symbols in red correspond to the current measurements obtained at $z/D = 45$ (◯), 50 (△) and 55 (□); and symbols in blue correspond to hot-wire measurements of WF69 at $z/D = 50$ (△) and 60 (□). The black line represents the least-squares spline obtained by PL93 for hot-wire measurements in the self-similar region. The hot-wire measurements were obtained by digitising the plots in the references.

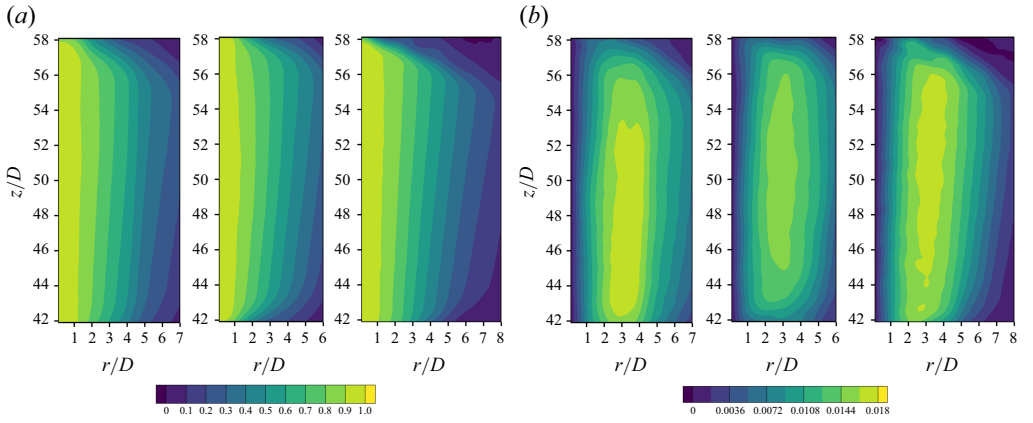

Figure 4. Contours of the (*a*) normalised mean axial velocity $\langle U_z\rangle/\langle U_{zc}\rangle$ and the (*b*) dominant Reynolds stress $\langle u_r u_z\rangle/\langle U_{zc}\rangle^2$ for $Re_D = 2640$ (left), 5280 (middle) and 10700 (right). The mean quantities are obtained by averaging over the azimuthal direction. Here, $\langle U_{zc}\rangle(z)$ is the local centreline axial velocity.

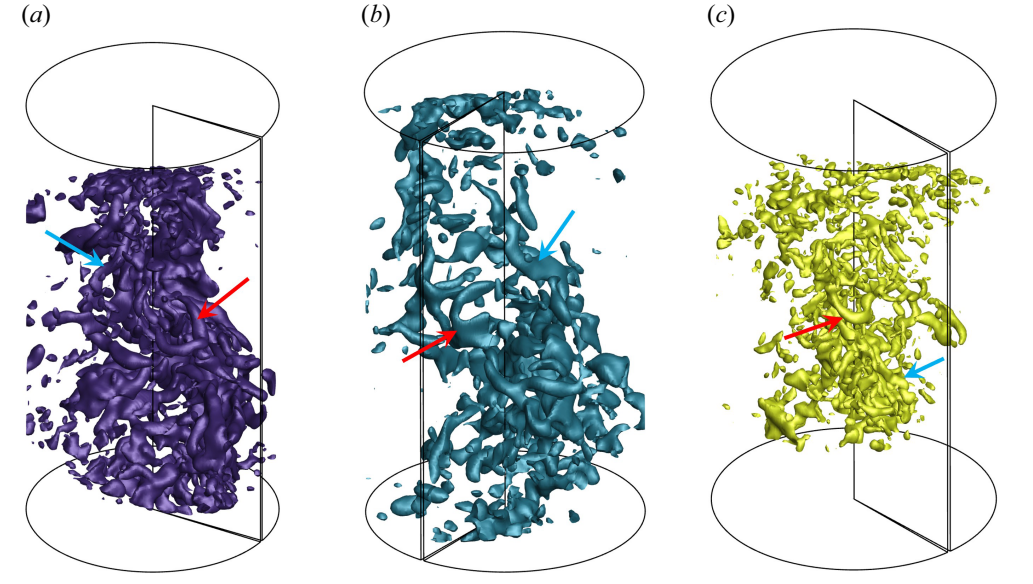

Figure 5. Instantaneous coherent structures visualised using iso-surfaces of vorticity magnitude for (*a*) *Re*2K with $|\widetilde{\boldsymbol{\omega}}| = 14\ \mathrm{s}^{-1}$, (*b*) *Re*5K with $|\widetilde{\boldsymbol{\omega}}| = 32\ \mathrm{s}^{-1}$ and (*c*) *Re*10K with $|\widetilde{\boldsymbol{\omega}}| = 75\ \mathrm{s}^{-1}$. The most prominent tubular structure and the C-shaped loop are indicated by blue and red arrows, respectively.

3.2. *Coherent vortical structures*

The coherent structures are visualised using iso-surfaces of vorticity magnitude $|\widetilde{\boldsymbol{\omega}}|$. Of the different criteria available to visualise coherent structures such as the Δ-, Q-, λ_2-criterion, in this study, we use the vorticity magnitude to visualise vortical structures in the jet. This choice is motivated by the superior accuracy with our measurement methodology, compared with other higher-order quantities such as the Q-method or the λ_2-criterion. For similar reasons, we have used the vorticity-magnitude criterion to visualise coherent structures in our previous studies on strained turbulence in contractions (Mugundhan *et al.* 2020; Mugundhan & Thoroddsen 2023; Alhareth *et al.* 2024*a*,*b*). Instantaneous

structures are shown in figures 2 and 5. At the lowest Reynolds number, we see long tubular structures inclined with respect to the axial direction (figure 5*a*). In contrast, shorter and finer structures emerge at higher Reynolds numbers, with prominent C-shaped structures around the axis. For a smooth inlet with a large contraction ratio, the near-field consists of vortex rings that arise due to Kelvin–Helmholtz instabilities in the laminar shear layer (Crow & Champagne 1971; Liepmann & Gharib 1992). These vortex rings are broken down into an assembly of C-shaped horseshoe vortices or long tubular structures, as they are advected downstream. Such horseshoe-shaped structures have been observed both in stereoscopic PIV measurements (Hori & Sakakibara 2004; Matsuda & Sakakibara 2005) and in direct numerical simulations (Suto *et al.* 2004; Samie *et al.* 2022). Samie *et al.* (2022) analysed the coherent structures in the near- and intermediate-fields up to $z/D = 25$ and identified horseshoe eddies, using conditional averaging based on their relative orientation. They defined an 'upright' eddy when its head is positioned away from the jet axis and its legs point upwards towards the axis. The opposite orientation, with the head positioned closer to the axis with legs pointing downwards away from the axis, was labelled an 'inverted' eddy. In our case, the inlet condition is a fully developed turbulent pipe flow and, hence, regular azimuthal vortex rings will not form. However, our three-dimensional measurements show that both the upright and inverted structures are observed even further downstream up to $z/D = 55$.

3.3. *Distribution of energy over Fourier modes*

Figure 6(*a*) shows the distribution of Λ^m for the first 51 azimuthal Fourier modes for the velocity and vorticity fields. We use the first 51 modes, since the value of Λ^m falls below $\sim$2 % to 4 % of its initial value at $m = 50$, for the highest Re case. The decay of Λ^m is even faster for the lower Re cases. These plots are obtained after removing the mean of the different independent realisations, for each Reynolds number Re. We have ten independent runs each for Re2K and Re5K, and 15 runs for the largest Re10K. The spectra of $\Lambda^m = \mathrm{diag}[\lambda_n^m]$; $n = [1, N]$ for the second mode $m = 1$, for all runs, are shown in figure 21. The overlap of the curves confirms the convergence and repeatability of the experiments. Figure 6(*a*) shows an increase in the value of Λ^m with an increase in the Reynolds number Re, as one would expect, due to stronger fluctuations at higher Re. The corresponding cumulative distribution, normalised by the sum over the 51 modes $\sum_{m=0}^{50} \Lambda^m$ is shown in figure 6(*b*). For velocity as the processed state vector, this ratio reaches a threshold fraction of 0.7 at $m = 4, 4$ and 5 for Re2K, Re5K and Re10K, respectively. The corresponding values of m for the same threshold for vorticity are $m = 8, 8$ and 11. We conclude that to express the vorticity field in a modal decomposition, it requires a larger number of azimuthal modes, when compared with the velocity field. Figure 6(*c*) shows the contribution of the first eleven m-modes to the total fluctuating energy and enstrophy of the flow. The first mode, $m = 1$, dominates the other modes, followed by $m = 0$ and $m = 2$ modes, and this behaviour is consistent across all included Reynolds numbers. The contributions of the higher modes decrease approximately as $1/m$. The percentage contributions of the different values of m for the intermediate case Re5K are summarised in table 3. Mullyadzhanov *et al.* (2018) report the contributions of the first ten Fourier modes in the far-field for a fully turbulent jet at $Re = 5940$, which is of the same order as our intermediate Re case. Their percentage contributions (k^m (%)) of the first ten modes are 11.5 %, 16.7 %, 13.1 %, 9.2 %, 6.7 %, 4.8 %, 3.7 %, 2.9 %, 2.4 %, 1.9 % and 1.6 %, respectively. Our observed contributions of the first four modes are 65 %, 35 %, 25 % and 16 % for Re5K, which are significantly higher than those reported by Mullyadzhanov *et al.* (2018). However, the contributions of the higher modes are similar to the earlier study.

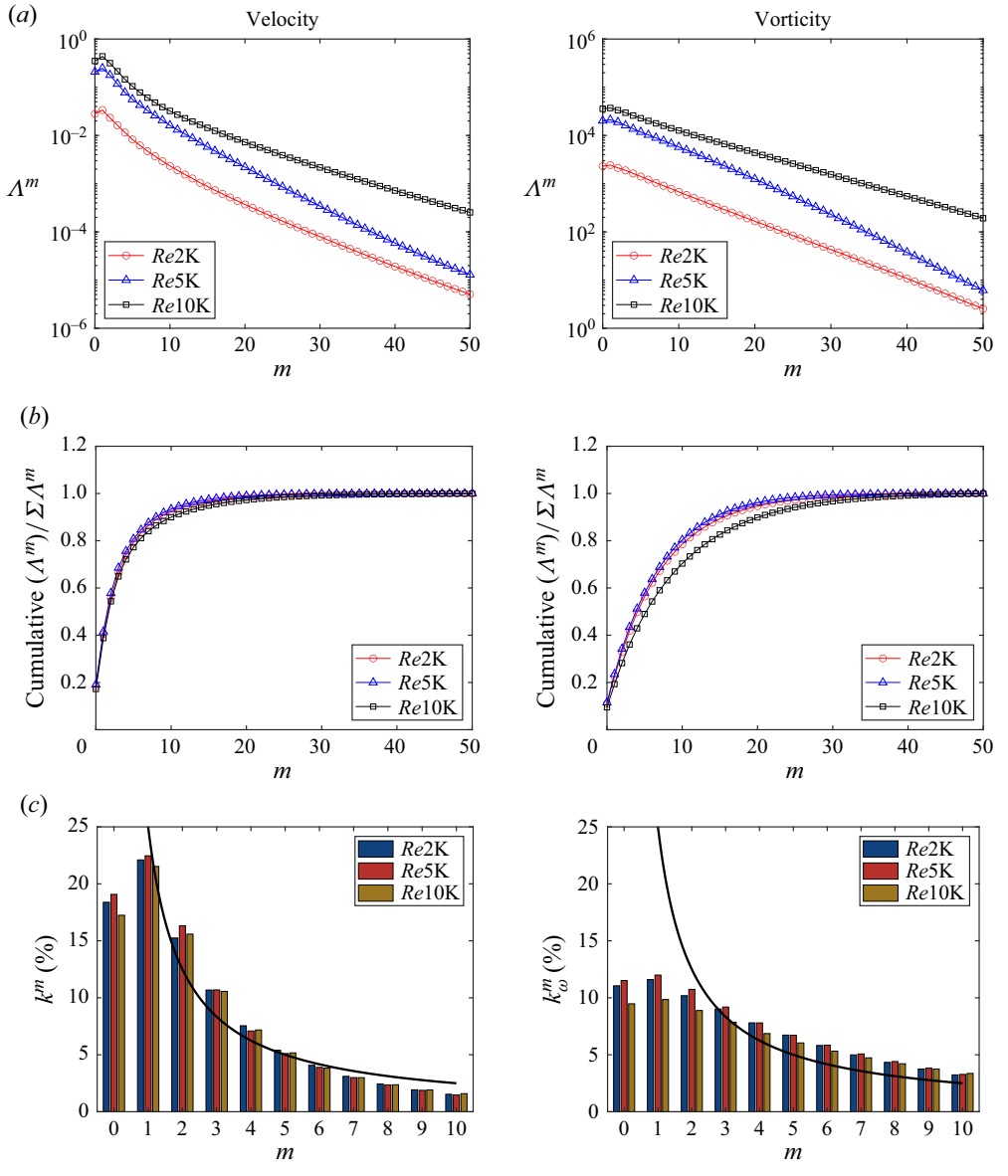

Figure 6. (*a*) Distribution of Λ^m, the eigenvalues of the correlation matrix, for the velocity fluctuations (left) and vorticity fluctuations (right), over the first 51 azimuthal Fourier modes, from $m = 0$ to $m = 50$. All three components of velocity (or vorticity) are included. The eigenvalues represent the fluctuation energy k^m (for velocity) and enstrophy k^m_ω (for vorticity). (*b*) Cumulative distribution of Λ^m shown in panel (*a*) taking the sum of the first 51 modes. (*c*) Percentage contribution of the different Fourier modes to the total energy (left) and total enstrophy (right). The black line in panel (*c*) is given by the equation $25/m$.

Figure 7 shows the relative contribution of the dominant five POD modes for each Fourier mode, for all three Reynolds numbers, for both velocity and vorticity. The contributions of the m modes for velocity decline faster compared with those based on vorticity, as displayed in figure 6. The first two POD modes contribute to 5 % to 10 % of the total fluctuation energy, with the most dominant $m = 1$ mode, as expected. However, they only contribute to 0.7 % to 1.5 % of the total enstrophy. We summarise the number

Mode	$m=0$	1	2	3	4	5	6	7	8	9	10
$k^m(\%)$	19.1	22.5	16.3	10.7	7.1	5.1	3.9	3.0	2.4	1.9	1.5
$k^m_\omega(\%)$	11.5	12.0	10.7	9.2	7.8	6.7	5.8	5.1	4.4	3.8	3.3

Table 3. Contribution of the first eleven azimuthal m modes to the total fluctuation energy k^m (%) and enstrophy $k^m_\omega(\%)$ for the intermediate Reynolds number Re.

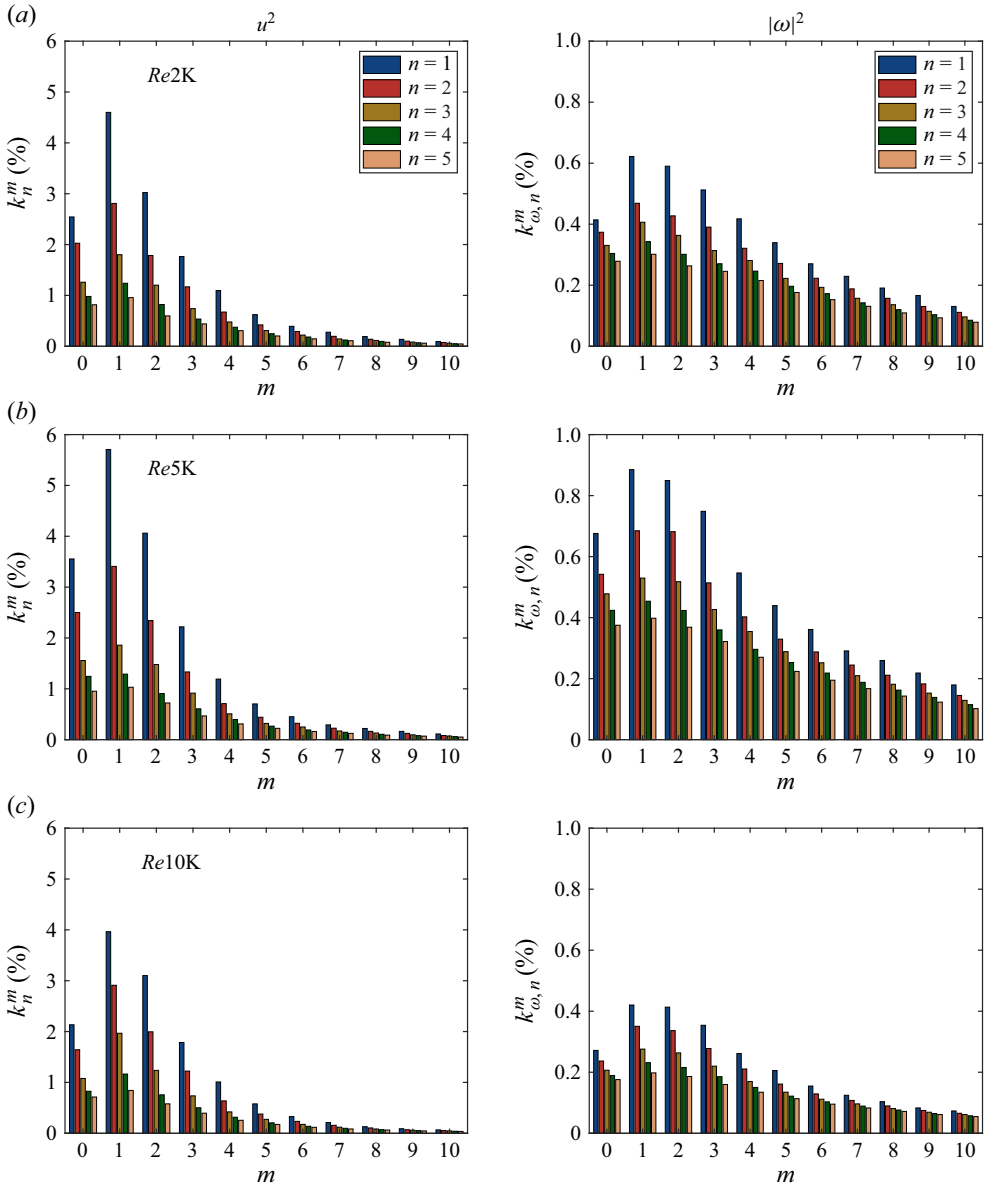

Figure 7. Contribution of the first five POD modes, for each azimuthal mode m, to the fluctuation energy k^m (left) and enstrophy k^m_ω (right) for cases (*a*) *Re*2K, (*b*) *Re*5K and (*c*) *Re*10K.

Case	*Re*2K	*Re*5K	*Re*10K	*Re*2K	*Re*5K	*Re*10K
Mode		$m=0$			$m=1$	
Velocity	19	13	25	14	9	16
Vorticity	57	40	74	54	37	70
Mode		$m=2$			$m=3$	
Velocity	17	10	18	20	13	24
Vorticity	53	36	69	53	37	70

Table 4. Number of POD modes which contribute to 70 % of the energy or enstrophy in each Fourier mode.

of POD modes needed to contribute 70 % of the total energy in table 4. The minimum number of POD modes for a particular azimuthal mode m is 13 (for velocity fields) and 40 (for vorticity fields) for the intermediate case *Re*5K, which has the largest number of snapshots in time (see table 2). With a longer time series, there is a higher likelihood of capturing the dominant structures. Such structures could possibly be missed in the other two *Re* cases that have fewer experimental snapshots.

3.4. *Shapes of the POD modes*

In this section, we further investigate the two dominant velocity POD modes, for the azimuthal modes $m=0, 1, 2$. These modes are presented in figures 8 to 11; the corresponding vorticity POD modes are displayed in figure 12. In either case, the modal shapes are shown after averaging over the many experimental runs for each *Re* selection. The POD of velocity fields for $m=1$ and $n=1$ for the *Re*10K experimental realisations, i.e. for the fifteen independent runs C1 to C15, is shown in figure 8(a). The spatial modes from all experimental runs show a helical structure around the axis, but are different in their azimuthal phase. This difference in phase could be due to a difference in starting phase between runs. As mentioned earlier, in our case, the time series length is limited by the camera memory. Hence, for better convergence, we average over many realisations after phase-rotating the modes with respect to a common basis. For *Re*10K, we choose C1 as the reference for a rotation, and the modes of other runs C2 to C15 are suitably rotated. The rotation operation is performed by minimising the following difference:

$$\| \mathcal{U}_i - \mathcal{U}_j \boldsymbol{R} \|, \tag{3.1}$$

where, $\mathcal{U}_i$, $\mathcal{U}_j$ are the full POD matrices (from (2.2)) for runs Ci and Cj, respectively, while $\boldsymbol{R}$ stands for a rotation matrix, which is obtained as

$$\boldsymbol{R} = \boldsymbol{P}\mathbb{Q}\boldsymbol{S}^H, \tag{3.2}$$

where $\boldsymbol{P}$, $\boldsymbol{S}$ are the factors of the triple decomposition of the matrix $\boldsymbol{M} = \mathcal{U}_2^H \mathcal{U}_1$. The actual singular value, $\boldsymbol{Q}$, in the factorisation $\boldsymbol{M} = \boldsymbol{P}\boldsymbol{Q}\boldsymbol{S}^H$, should be an identity matrix $\boldsymbol{I}$. To ensure orthogonality of the rotation matrix $\boldsymbol{R}$, i.e. satisfies $\boldsymbol{R}\boldsymbol{R}^T = \boldsymbol{I}$, matrix $\boldsymbol{Q}$ is replaced by a modified matrix $\mathbb{Q}$, which is given by

$$\mathbb{Q} = \begin{bmatrix} 1 & 0 & 0 & \dots & \dots & 0 \\ 0 & 1 & 0 & \dots & \dots & 0 \\ \dots & \dots & \dots & \dots & \dots & 0 \\ 0 & 0 & 0 & \dots & 1 & 0 \\ 0 & 0 & 0 & \dots & \dots & \det(\boldsymbol{P}\boldsymbol{Q}^H) \end{bmatrix} \tag{3.3}$$

with det as the determinant.

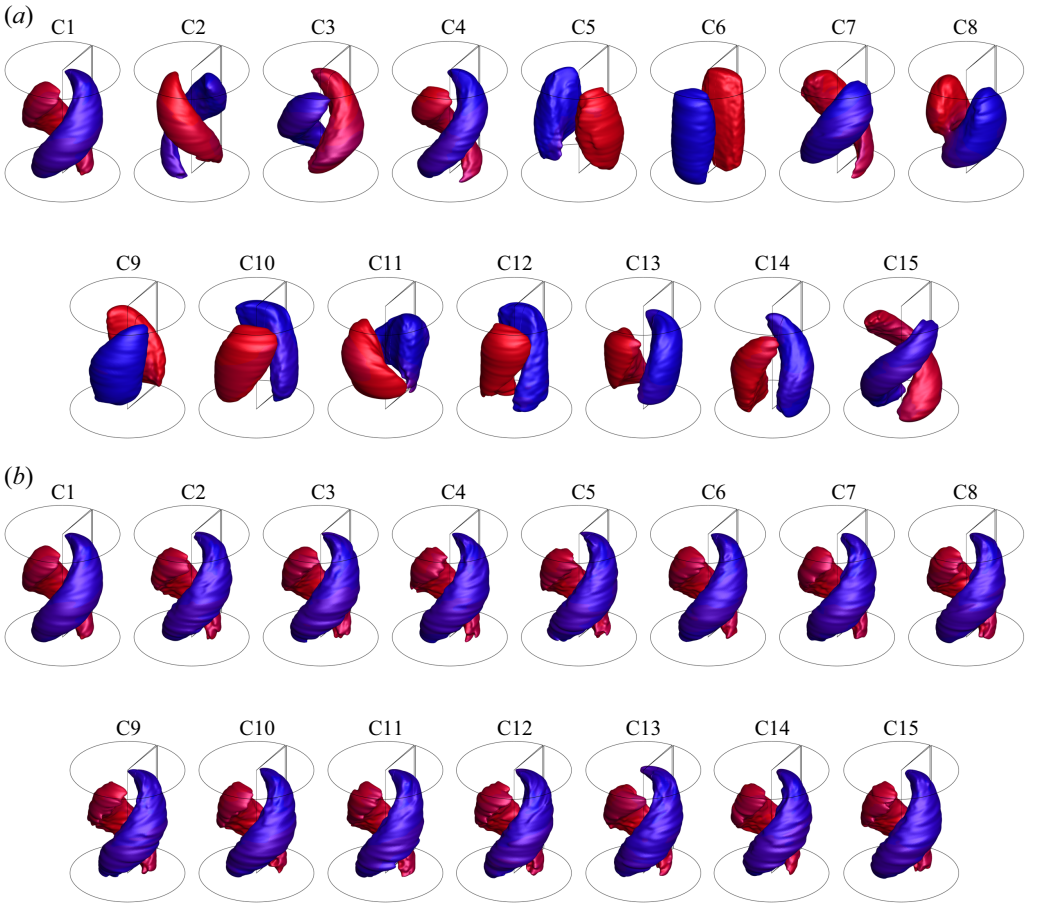

Figure 8. (*a*) Actual POD modes ($m = 1, n = 1$) extracted using velocity fluctuations from the fifteen independent experimental runs for the $Re10$K case. The POD is represented by iso-surfaces of velocity magnitude, $|\boldsymbol{U}| = 0.01$, coloured by the axial velocity. The colours represent the opposite directions of the axial velocity. (*b*) Modes corresponding to panel (*a*) after rotation in modal space with respect to the base case (C1).

The $n = 1$ POD modes, applying this rotation, are shown in figure 8(*b*). After this rotation, the modes for all experimental runs are phase-synchronised in the azimuthal direction and hence can be averaged. The primary and secondary POD modes, for $m = 1$, averaged in the above way, are shown in figure 9, for all three Reynolds number cases. All Re numbers show the helical structures in both modes, but there is a difference in the helix direction. Similar helical POD structures for $m = 1$ have been reported by Mullyadzhanov *et al.* (2018), based on the DNS of a turbulent jet issued from a fully developed pipe with a co-flow. The POD modes have been visualised at $Re = 5940$ and in the region $z/D = 30$ to 40, i.e. slightly upstream of our current measurement locations. Tso & Hussain (1989) identified axisymmetric, helical and double-helical structures in the far-field of a jet, measured by a rake of X-wires in combination with invoking Taylor's hypothesis. They report that, among the three classes of structures, the helical structures were dominant, which corroborates the emergence of the same structures as primary POD modes. Yoda *et al.* (1994), based on their three-dimensional (3-D) concentration measurement of a turbulent round jet (natural, excited and buoyant at $Re = 1000-4000$),

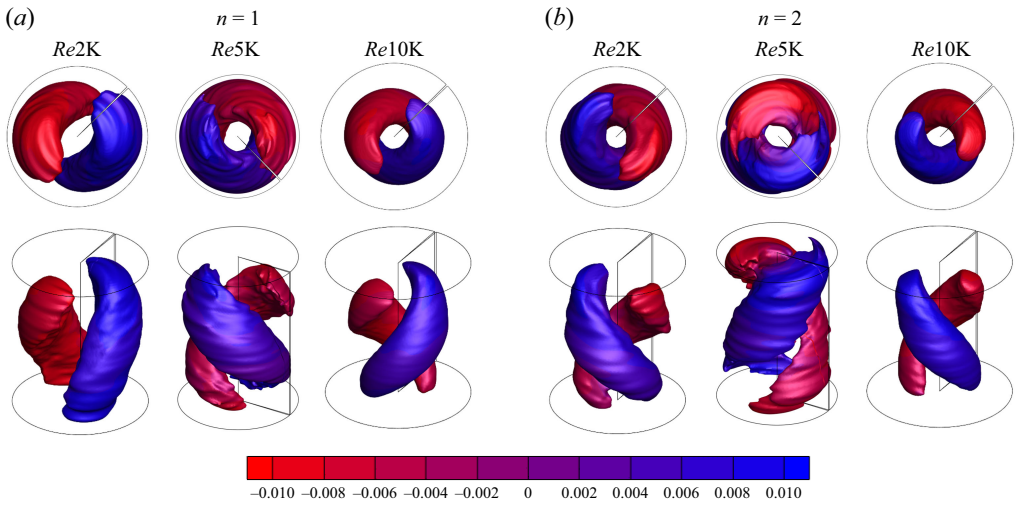

Figure 9. Top and isometric views of POD modes represented by iso-surfaces of the velocity magnitude, $|\boldsymbol{U}| = 0.01$, coloured by the axial velocity for the most dominant azimuthal mode $m = 1$ and (a) $n = 1$ and (b) $n = 2$. The geometry is not to scale. The regions with no vectors at the top and bottom edges are trimmed.

concluded that the far-field consisted of a pair of counter-rotating helices and did not consist of expanding spiral proposed by Dimotakis *et al.* (1983). They corroborated the 3-D concentration structures obtained by the scanning-planar laser-induced fluorescence (PLIF) technique, with sectional views. This conclusion is inline with the linear stability theory which predicts the helical mode to be the most unstable mode in the far-field. Also, the counter-rotating helical modes together can alone result in symmetric and anti-symmetric images on two-dimensional (2-D) slices of the jet. They also proposed that these helices could be due to the vortex reconnection of tilted-vortex rings of the near-field. Note that for $m = 1$, the velocity PODs change sign across the axis. It is also interesting to note that the instantaneous coherent structures, visualised by isosurfaces of vorticity magnitude in our measurements, show helical patterns of structure ejections into the measurement domain, together with their subsequent advection downstream. In contrast, the instantaneous structures we see in our study are dominated by tubular or C-shaped structures. It is notable that the *Re*2K and *Re*10K cases have smoother POD structures compared with the intermediate *Re*5K case, which we attribute to the shorter Δt between the volumes (snapshots) with *Re*5K, which results in samples with a higher temporal dependency. Cases *Re*2K and *Re*10K have a temporal snapshot spacing Δt of approximately 9 to 12 times larger than that of *Re*5K. Hence, the snapshots used to construct the data matrix $\mathcal{D}$ are statistically less dependent. The $m = 0$ mode has no azimuthal wavelength and is therefore a structure of revolution about the axis, see figures 10(a) and 10(b). The $m = 2$ mode shows streamwise helices with a weaker twist compared with the corresponding $m = 1$ mode, see figure 9. The first and second modes for $m = 2$, in figures 10(c) and 10(d), demonstrate that the secondary mode has smaller structures compared with the first one.

The structure corresponding to the radial velocities u_r are also helical but appear flatter, with a smaller helix angle, compared with the absolute velocity structures, visualised in figure 11, for $m = 1$. The radial velocity structures extend all the way to the axis. The radial gap we observe is due to the interpolated cylindrical domain which has a finite radius ϵ_r at the axis for ease of interpolation. The helix angles for the u_r structures, with respect to the horizontal, are measured to be 34°, 27° and 31° for *Re*2K, *Re*5K and *Re*10K, respectively.

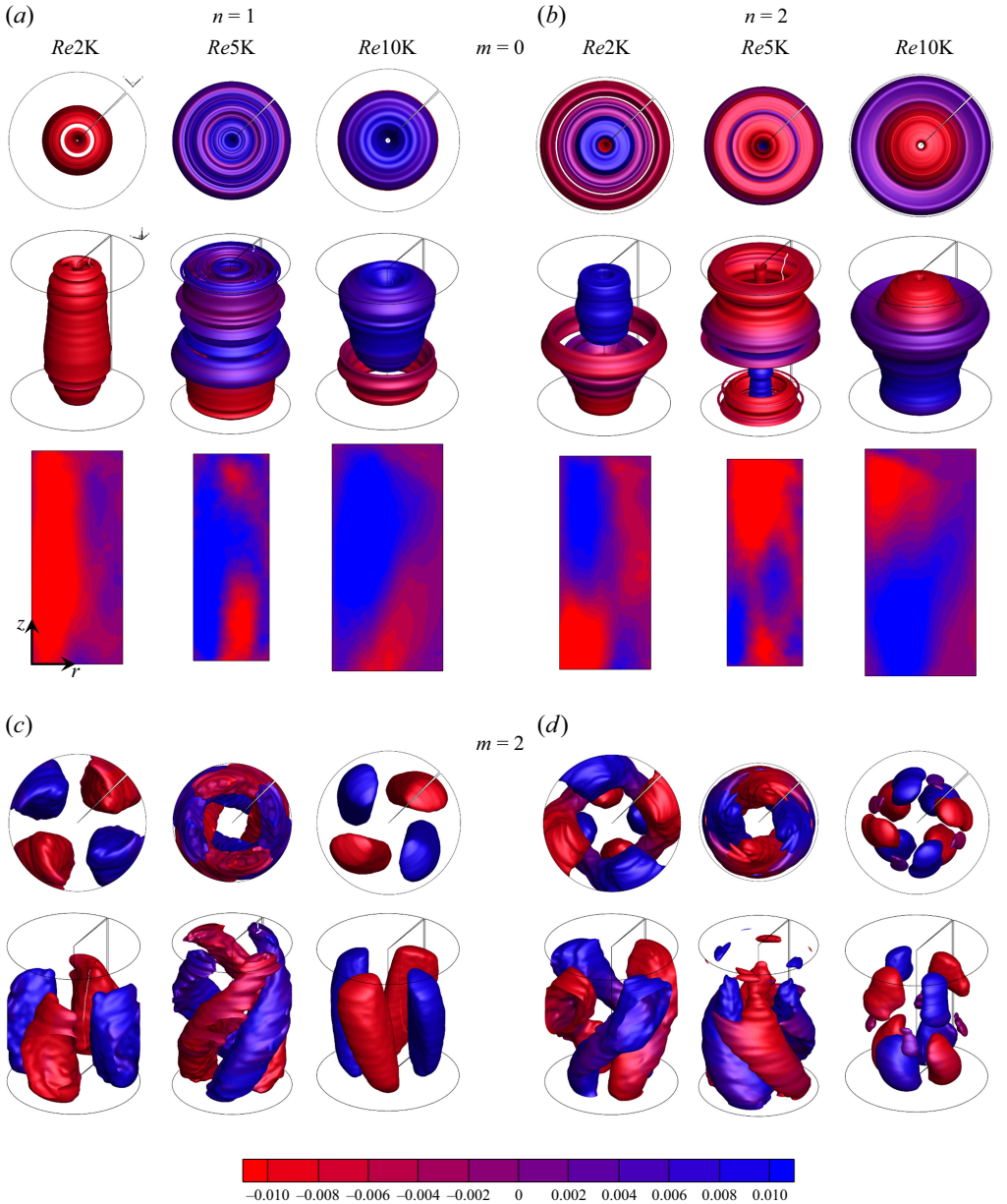

Figure 10. POD modes represented by iso-surfaces of the velocity magnitude, $|\boldsymbol{U}| = 0.01$, coloured by the axial velocity for the most dominant azimuthal mode (*a,b*) $m = 0$ and $n = 1$, 2, and (*c,d*) $m = 2$ and $n = 1$, 2. The r–z projection of the ($m = 0$) modes is also included in panels (*a*) and (*b*).

The corresponding values for absolute velocity structures are larger at 46°, 31° and 35°, respectively. Hence, by virtue of their smaller helix angles, the u_r-structures complete one full revolution about the axis in the measurement domain. The corresponding axial distance between the positive and negative peaks of the u_r-modes in the r–z-plane are approximately 55 mm, 40 mm and 40 mm, respectively. However, for the u_z-modes, they are approximately 65 mm, 45 mm and 50 mm, respectively.

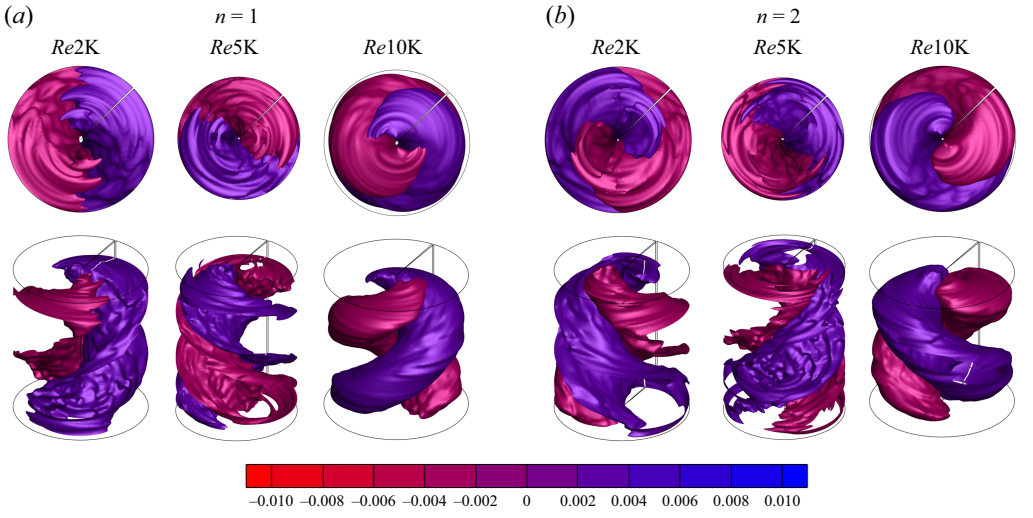

Figure 11. POD modes represented by iso-surfaces of the radial velocity, $U_r = \pm 0.0025$, coloured by the axial velocity for the most dominant azimuthal mode $m = 1$ and (a) $n = 1$ and (b) $n = 2$.

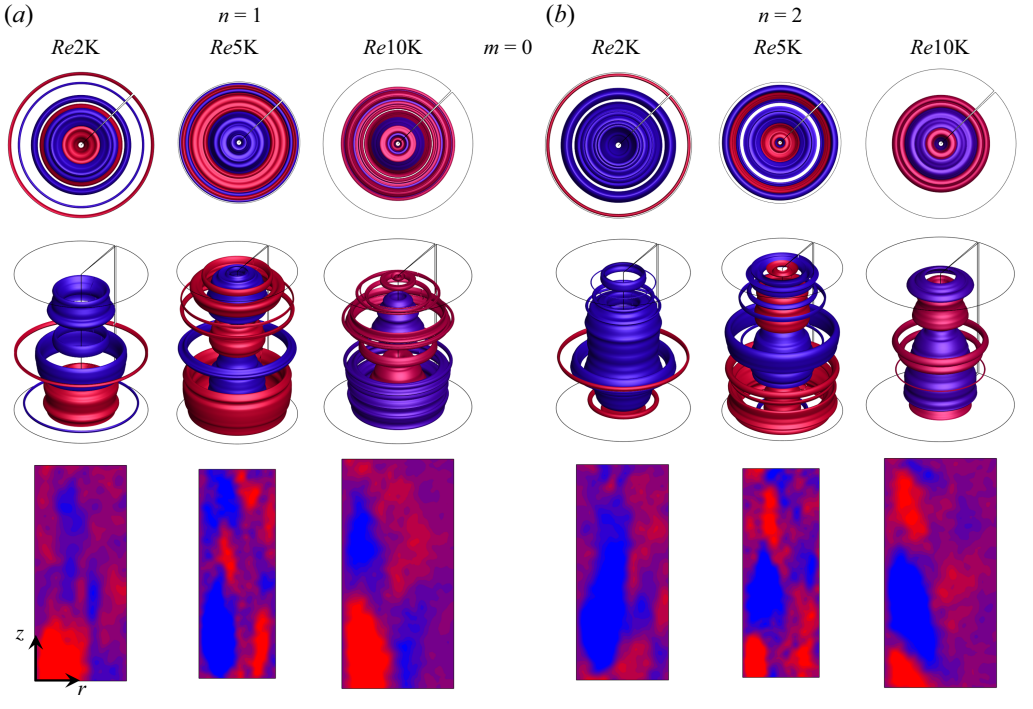

Figure 12. For caption see next page.

3.5. *POD of vorticity*

We continue by performing the POD analysis on the vorticity field and the $m = 0, 1, 2$ modes, which contribute to approximately 30 % of the total enstrophy, are presented in figure 12. The axisymmetric $m = 0$ mode consists of rings of different radii around the axis, populating the entire radial extent of the domain. The choice of the iso-surface

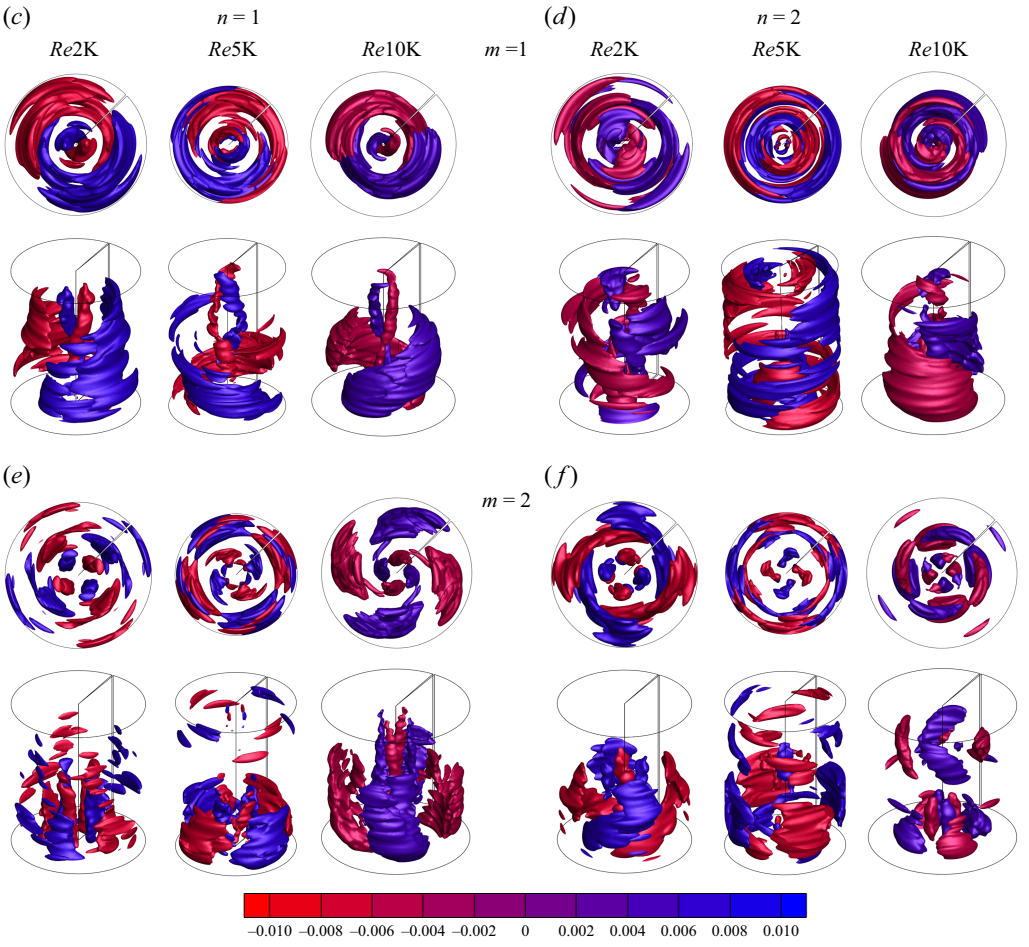

Figure 12. (cntd). POD modes represented by iso-surfaces of the azimuthal vorticity, ω_θ, coloured by the same quantity for the modes (*a*,*b*) $m = 0$ and $n = 1, 2$, (*c*,*d*) $m = 1$ and $n = 1, 2$, and (*e*,*f*) $m = 2$ and $n = 1, 2$. The threshold values of ω_θ for *Re*2K, *Re*5K and *Re*10K are 0.0065, 0.0075 and 0.0055 $\mathrm{m}^{3/2}\ \mathrm{s}^{-1}$, respectively. The r–z-projections of the $(m = 0)$-modes are also included in the bottom row of panels (*a*) and (*b*). To highlight the cylindrical axial structures in panel (*d*), we use lower threshold values of 0.0055, 0.0065 and 0.0045 $\mathrm{m}^{3/2}\ \mathrm{s}^{-1}$ for *Re*2K, *Re*5K and *Re*10K, respectively, in this panel.

values for the three different Reynolds numbers is distinct, owing to the difference in the $m = 0$ mode contribution to the enstrophy, as shown in figure 7. The higher Fourier modes are characterised by azimuthal C-shaped structures around the axis, representative of the horseshoe vortices reported in the far-downstream region of a turbulent jet by Suto *et al.* (2004), Matsuda & Sakakibara (2005), Casey *et al.* (2013) and Samie *et al.* (2022). Tinney *et al.* (2008*b*) showed that the $m = 0$ mode consisted of circular rings in the near-field ($z/D = 3$) when visualised by Q-iso-surfaces (i.e. the second invariant of the velocity gradient tensor); the authors labelled these modes as the jet column mode. Note that they constructed these structures from three-dimensional velocity measurements in a transverse plane while using Taylor's hypothesis with a constant axial convection velocity, thereby intertwining space and time coordinates without an explicit downstream evolution. The addition of the helical $m = 1$ mode broke down the rings into spiralling compact vortex tubes, which became more compact with a further addition of the $m = 2$ mode.

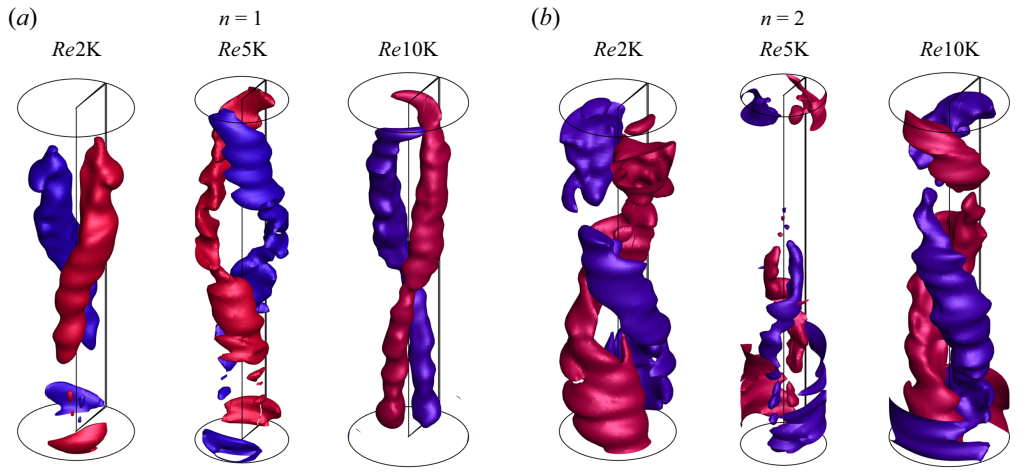

Figure 13. Cropped images of the POD modes from figure 12(*c, d*), to show the inner structures of ω_θ close to the axis of symmetry, for mode $m = 1$ and (*a*) $n = 1$ and (*b*) $n = 2$. The streamwise-oriented POD structures are shown in a cropped cylinder with radius of 30 % to 35 % of the original radius of the full domain. For thresholds of the iso-surfaces, refer to the caption of figure 12.

These structures become more disorganised further downstream, as expected considering the rather large Reynolds number of $Re = 10^6$. In a previous analysis of our scanning data, Casey *et al.* (2013) identified instantaneous tubular and loop structures, using vorticity magnitude as the state vector, and tracked and characterised their evolution. Violato & Scarano (2013) performed a POD analysis on the vorticity field obtained in the near-field ($z < 10D$) of a turbulent jet using the Tomo-PIV technique. The primary POD mode pairs of azimuthal vorticity, contributing to 11 % of the total enstrophy, describe the travelling ring vortices and had a characteristic Strouhal number of $St = 0.36$. Note that the analysis was performed using 500 independent snapshots with velocity fields obtained by correlation with interrogation size of 0.5 mm. Recent DNS work of Samie *et al.* (2022), based on conditional averaging, verified the existence of two different horseshoe structures with different orientations – eddies with heads close to the jet axis and heads pointing away from the jet axis. Another feature observed for the $m = 1$ and $m = 2$ vorticity modes is a pair of axially oriented, tubular structures of opposite signs, twisting around the jet axis. These structures are displayed more prominently in the cropped images shown in figure 13.

The iso-surfaces of the PODs representing the axial vorticity ω_z for $m = 1$ is shown in figure 14. The modes are characterised by conical structures with a moderate twist about the jet axis. These manifest themselves as inclined long streaks in the r–z-plane, with alternate signs. The primary $n = 1$ POD mode consists of a larger cone twisted around the axis, while the $n = 2$ structure contains at least two smaller conical components. The structures appear smoother and more continuous for the *Re*2K and *Re*10K cases, when compared with those for *Re*5K. The $n = 2$ mode for *Re*5K appears more disconnected, which could be attributed to the smaller Δt for that data set, compared with the data for the other Reynolds numbers.

3.6. *Dynamics of the POD modes*

After investigating the spatial composition of the POD modes across different modal numbers and azimuthal wave numbers, we now turn our attention towards the evolution of the time coefficients a_n^m to characterise the dynamics of the POD modes. We restrict

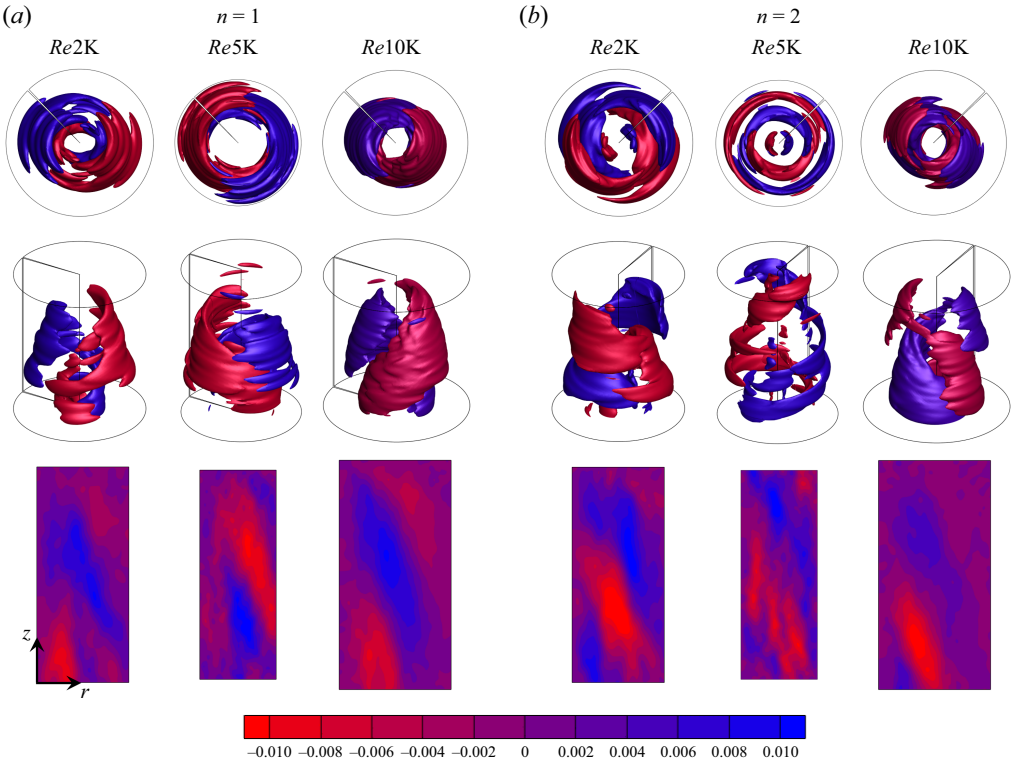

Figure 14. POD modes of axial vorticity ω_z for the $m = 1$ azimuthal Fourier mode, presented by iso-surfaces on the top row and as r–z-projections in the bottom row. The cross-sections are coloured by the same quantity, for the modes (*a*) $n = 1$ and (*b*) $n = 2$. The threshold values of the iso-surfaces for *Re*2K, *Re*5K and *Re*10K are 0.0065, 0.0075 and 0.0055 $\mathrm{m}^{3/2}\mathrm{s}^{-1}$, respectively.

this analysis to the best time-resolved case, *Re*5K, as the time step between volumes is larger for the remaining two cases, making it more challenging to capture the characteristic frequencies. The complex coefficients $a_n^m(t)$ are decomposed in the following manner, $\beta(t)e^{i\gamma t}$, where $\beta(t) = |a_n^m(t)|$ denotes its absolute amplitude and γ stands for its phase in the complex plane. The variation of the magnitude of the coefficients $\beta(t)$ with time, for the first two POD modes for $m = 1$, is shown in figure 15(*a*). Figure 15(*b*) shows the cumulative phase of the coefficients. The magnitude shown in figure 15(*a*) is given by the radius of the loci of the coefficients in the complex plane, which is shown in figure 15(*c, d*). Both the radius and the phase of these coefficients are computed with respect to their local centre of curvature, which can move about the coordinate centre. The cyclic motion of the coefficients in this plane indicates the helical motion of the corresponding mode (Davoust, Jacquin & Leclaire 2012; Mullyadzhanov *et al.* 2018). Davoust *et al.* (2012) analysed the first two Fourier modes of velocity in the near-field of a turbulent air jet from a wind tunnel. They used a high-speed stereo-PIV technique to measure the velocity field in a cross-sectional plane at $z/D = 2$ and argued that a circular pattern of these coefficients in the complex plane is representative of a global rotation or helical motion of the jet. The helical motion would also give rise to linear variations in the phase of these coefficients, which we observe in our analysis as well, see figure 15(*b*). Both modes exhibit a circular pattern with varying centres of curvature and, hence, we compute the phase of these complex numbers with respect to its local centre of curvature. The slope of

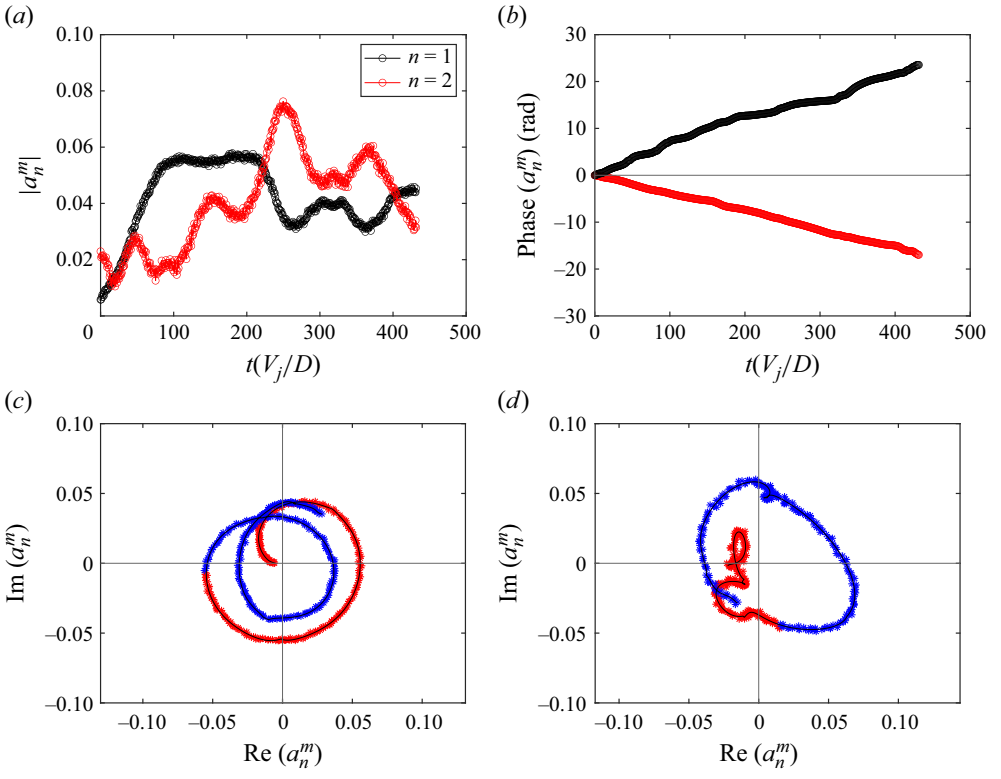

Figure 15. (*a*) Magnitude of the time coefficients a_n^m for the first two POD modes for $m = 1$, and (*b*) the cumulative phase of these coefficients' variation with time. (*c*,*d*) Time coefficients represented on the real-imaginary planes. The colour of the symbols in panels (*c*,*d*) is used to indicate the tracking direction with time. The time series starts with red and ends with blue. The thin black line is the sixth-order polynomial parametric fit to the coefficients.

this phase finally furnishes the frequency $f = \mathrm{d}\gamma/\mathrm{d}t$ associated with the precession of the modes about the jet axis. We see that the cumulative phase for the first two modes, which are mirror images of each other, have opposite slopes, implying an opposite direction of rotation – a feature that is consistently observed in all ten experimental realisations. Similar variations in the time-coefficient phase have been reported in turbulent channel flow (Sirovich, Ball & Keefe 1990), pipe flow (Duggleby *et al.* 2007) and jet flow with a co-flow component (Mullyadzhanov *et al.* 2017, 2018).

We estimate the frequency by fitting a line to this variation in phase, from graphs shown in figure 15(*b*). Once normalised by the nozzle diameter D and the jet inlet velocity V_j, we recover a Strouhal number (non-dimensionalised frequency) defined as $St = fD/V_j$. The frequency of the first five POD modes averaged over all ten runs, for $m = 0$ to $m = 9$, for velocity and vorticity fields, is shown in figures 16(*a*) and 16(*b*), respectively. For the velocity field, the higher POD modes show a slightly higher frequency than the lower Fourier modes. However, this difference tends to decrease and the frequency of $n = 2, 3$ modes tends to approach a constant at $St \approx 0.06$ for higher Fourier modes. Amongst the considered POD modes, the large-scale and first dominant POD mode, $n = 1$, precesses with lowest frequency and shows a gain in its frequency with an increase in the azimuthal wave number m. Mullyadzhanov *et al.* (2018) report St to be the same for modes $m = 1$ and $n = 1, 2$, which is approximately $St = 0.05$. However, in our case, the corresponding

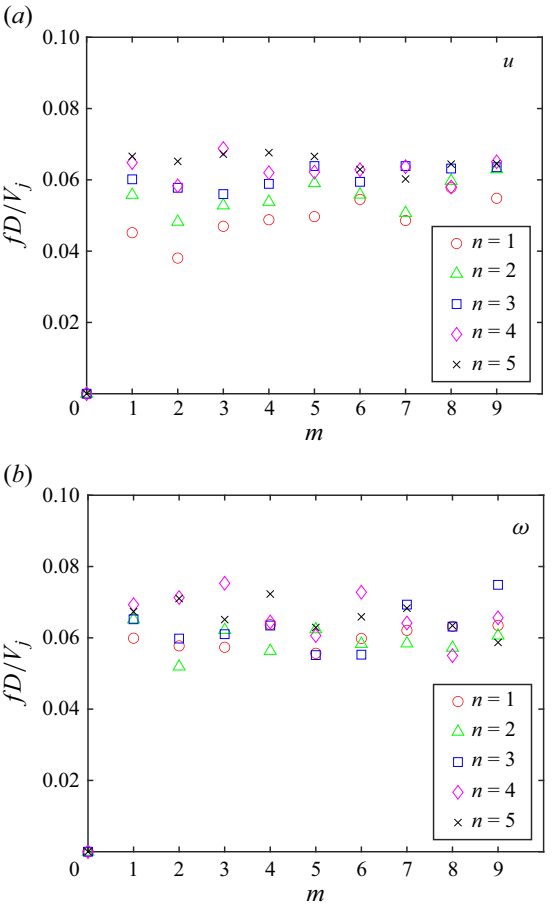

Figure 16. Precession frequency f of the (a) velocity POD modes, (b) vorticity POD modes for the first ten azimuthal Fourier modes. The frequency f is calculated as the slope of the cumulative phase. The cumulative phase for one case ($Re5$K) is shown in figure 15(b).

values are 0.05 and 0.06, respectively. The vorticity field shows a range of frequencies, with an average value of approximately $St = 0.07$.

3.7. *Flow field reconstruction using POD modes*

As a final step in our analysis, we attempt to reconstruct the flow field by summing over the most dominant modal components. This exercise is intended to reduce the original data set to the most energetic and coherent dynamic process. In particular, we perform the reconstruction of the fluctuating velocity for Fourier mode $m = 1$ using (2.3) and varying the number of POD modes. The reconstructed field based on adding two modes $n = 1, 2$ (indicated as $1 + 2$) contains approximately 40 % of the kinetic energy and using three modes $n = 1, 2, 3$ (indicated as $1 + 2 + 3$) captures approximately 50 % of the kinetic energy. They are displayed in figure 17 for one of the realisations, for a few selected time steps. A video of the complete time evolution, for one experimental run, is included in the Supplementary movie 1, and reader is urged to consult the animation. We see that the reconstruction consists of the characteristic helical POD structures, shown in figure 9, for both $n = (1 + 2)$ and $n = (1 + 2 + 3)$. The coherent structures rotate about the jet axis, as discussed in the previous section, and slowly advect in the mean flow

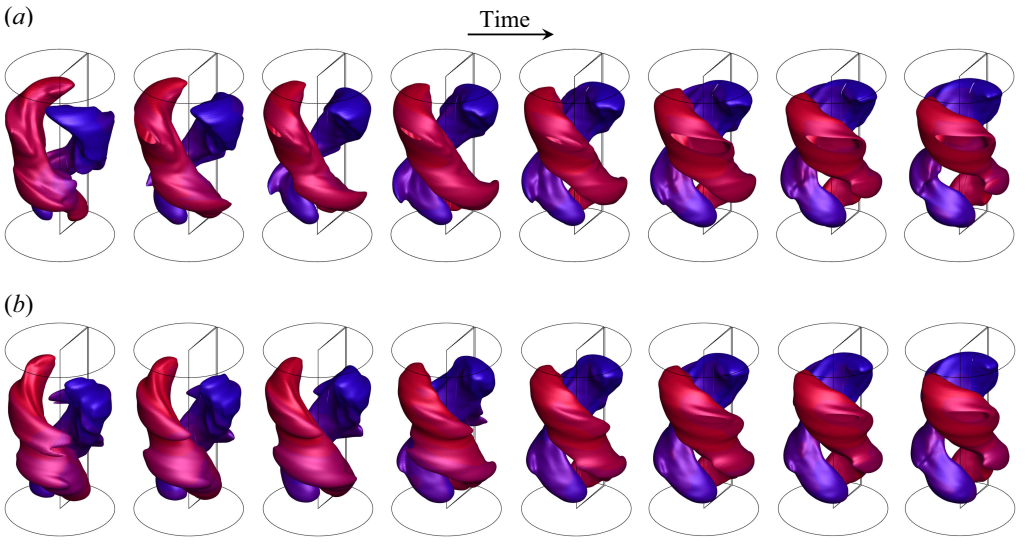

Figure 17. Time evolution of a partial reconstruction of the fluctuating velocity vector field for $m = 1$ at $Re5K$. The reconstruction used only two or three POD modes, (*a*) modes $n = (1 + 2)$ and (*b*) $n = (1 + 2 + 3)$. Both panels (*a*) and (*b*) correspond to the same time sequence, and the images are separated by $10\Delta t$. The reconstructed field is visualised by iso-surfaces of velocity magnitude and the two colours represent the signs of the axial velocity. The time-evolution videos, using the sum of one up to four POD modes, are included in the Supplementary movies 1 and 2, for $Re5K$ and $Re10K$ respectively.

direction. The reconstruction with three POD modes, shown in figure 17(*b*), are essentially indistinguishable from the reconstruction with two POD modes. Nonetheless, higher-order POD modes include more of the finer-scale details of these structures; the key features, however, are well captured by the first two or three POD modes.

We next show instantaneous snapshots of the reconstructed fields in figure 18, for Fourier modes $m = 0$ and $m = 1$. The reconstruction considers ten POD modes contributing to 70 % of the kinetic energy for each Fourier mode. The ω_θ structures constitute rings for the $m = 0$ mode and C-shaped structures in the case of $m = 1$, with both positive (green) and negative (indigo) azimuthal orientations. The axial velocity (u_z) structures (in red and blue) are characteristically more voluminous and appear on the inner or outer side of the ω_θ-rings, depending on their direction. We identify the prominent u_z-structures in figure 18. In figure 18(*a*), we first consider the $m = 0$ mode which shows the spatial relation between the axial velocity u_z and the underlying azimuthal vorticity ω_θ. Figure 18(*b*) only shows the vortex rings for the same case. The green coloured positive ω_θ-ring induces a positive axial velocity u_z (in blue) on its inner side and a negative u_z (in red) on its outer side; in effect, this vorticity transports the high-speed fluid to the outer region away from the axis. Conversely, the negative ω_θ-ring induces a negative u_z (in blue) on its inner side and positive velocity u_z (in red) on its outer side. This is evident for the negative u_z-structure S_1, which appears on the inner side of the negative ω_θ-rings V_1 and V_3, and on the outer side of the positive ω_θ-rings V_2 and V_4. However, a positive u_z structure S_3 appears between the positive ring V_6 and the negative ring V_7. Similar positioning of negative u_z-structures S_2, S_6 and S_7, and positive u_z-structures S_4 and S_5 with respect to vorticity rings can be seen in both modes. Reconstruction, considering POD modes that contribute 60 % and 80 % of total energy/enstrophy, shows very similar correspondence between the velocity and vorticity structures. The instantaneous reconstructed images at two different instants for 60 %−80 % are included in figure 24. The large-scale features

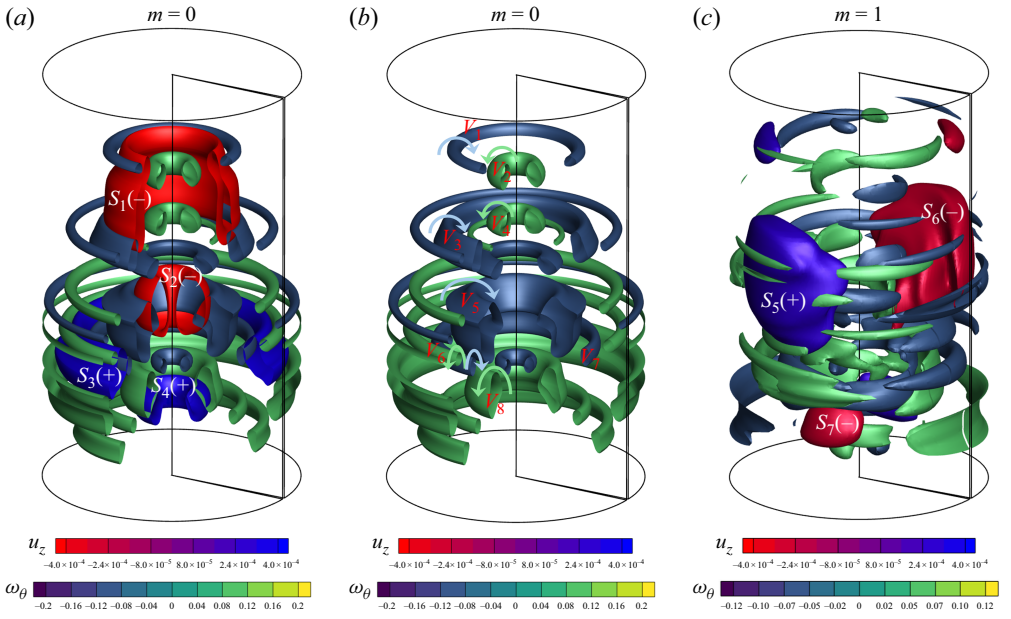

Figure 18. Instantaneous reconstructed images of u_z superimposed on ω_θ for (a,b) $m = 0$ in and (c) $m = 1$. The reconstruction is shown for one instant of $Re5K$, and is accomplished using ten POD modes for the velocity field and 37 modes for the vorticity field, which contribute 70 % of the energy and enstrophy, respectively. The prominent structures corresponding to u_z are labelled (S_1 to S_7) and their direction is indicated in the brackets: positive for upward motion (in blue) versus negative for downward motion (in red). The reconstruction for $m = 0$ is shown in 75 % of the full domain for more internal details near the axis in panels (a,b). The same reconstruction is shown in panel (b) with only the ω_θ rings. Vortex rings associated with structures S_1 to S_4 in panel (a) are labelled V_1 to V_4, and their directions are marked with arrows. Videos of the time evolution of the reconstruction, over the full recording cycle of one experimental run, are included in the Supplementary movie 3.

for all three cases look very similar, with the case having 80 % energy capturing more features compared with the remaining two.

The continuous induction of u_z-structures by the azimuthal rings occurs throughout the run in the time evolution videos (see Supplementary movies 3–4). The videos show that the large-scale u_z-structures get propagated through the entire length of the domain approximately four times during the full time-record.

To investigate the phase relation between the velocity and vorticity modes, we compare the magnitude and phase of the time coefficients for the first two velocity and vorticity modes in figure 25, for $m = 1$ corresponding to the case presented in figure 18(c). The instantaneous phase of the coefficients of $\boldsymbol{u}$ and $\boldsymbol{\omega}$ match reasonably well, as seen in figure 25(b). This match is even more prominent when we consider the cumulative phase, as shown in figure 25(c). The higher slope in the vorticity mode indicates a larger characteristic frequency, as reported in § 3.6. It is noteworthy that the direction of rotation of $\boldsymbol{u}$- and $\boldsymbol{\omega}$-modes is the same, for a given n, in this experimental run. A similar comparison with other experimental runs showed that the matching of the rotation direction of $\boldsymbol{u}$- and $\boldsymbol{\omega}$-modes, for identical n, is less conclusive. However, the $n = 1$, 2-modes of $\boldsymbol{u}$ always have an opposite sense of direction. This is also true with the first two modes of $\boldsymbol{\omega}$ in nine out of ten cases.

The 'information content' of the data matrix $\mathcal{D}$ can be probed by analysing the sum of its singular values $\Sigma_i \sigma_i$, also referred to as its nuclear norm. This test will help establish

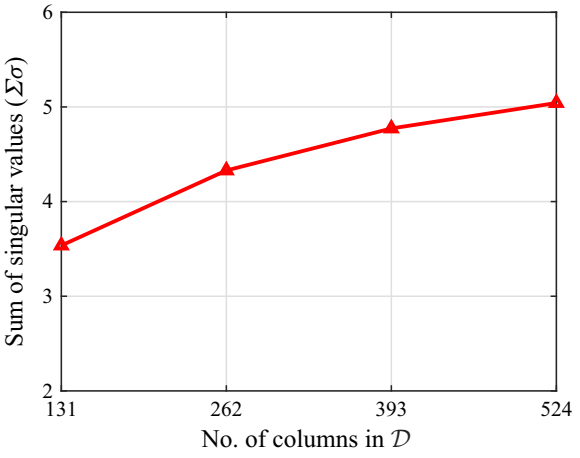

Figure 19. To characterise the degree of linear independence of the snapshots in the data matrix $\mathcal{D}$, the sum of the singular values for three different data lengths, using different fractions of the full data set $\mathcal{D}$, is plotted against the number of columns used. The columns are constructed with the velocity fluctuations for $m = 1$ and *Re*5K. The plot shown is the average over results obtained from the ten different experimental runs.

if the size of the data matrix, i.e. the number of snapshots, is sufficient to fully capture the dynamics of the flow, as it is directly linked to a measure of dependence of the columns of $\mathcal{D}$. We perform the sum over singular values for different column numbers of the full data matrix. The original matrix $\mathcal{D}$ has a total of 524 columns, which we compare with sums over shorter segments of 131, 262 and 393 columns, thereby using 25 %, 50 %, 75 % and 100 % of the time series. The resulting sums of the singular values are plotted in figure 19. This sum $\Sigma_i \sigma_i$ tends to a constant value with an increase in the number of columns, with the difference between consecutive pairs reducing as 0.8, 0.44 and 0.27, respectively. This monotonic reduction in the difference indicates diminishing returns from including additional snapshots; in other words, sampling more data will increasingly duplicate information that is already contained in the current data matrix. In addition, using convergence acceleration techniques on the nuclear norms (from figure 19) reveals that the curve asymptotes towards a value of 5.32, which confirms that the 524-snapshot dataset used in this study contains an estimated 94.9 % of the full information content. Note that the results shown in the figure have been obtained by averaging over the ten different experimental runs. Thus, we can conclude that the 524 consecutive snapshots used in this study are sufficient to characterise the POD modes of the flow.

4. Discussion and conclusions

In this investigation, we applied a Fourier-based POD modal analysis to the time-resolved volumetric measurements of a fully turbulent jet. This analysis included the extraction and interpretation of the dominant structures of velocity and vorticity in the far-field of the jet, around an axial location of $z/D \simeq 50$. The limited memory of the cameras curtails the total duration of each recording, and hence, to produce converged POD modes, we developed and applied a novel method of averaging over many realisations. In this averaging procedure, the modes from different realisations have been phase-aligned by an optimal rotation with respect to a common POD modal basis. This method could be suitable beyond the scope of this paper, when analysing coherent structures

in measurements wherein the time duration of recording is limited – such as in image-based methods where, for CMOS cameras, we typically have to contend with a trade-off among the number of voxels, the frame rates and the total duration of clips. It is worth mentioning that many modal analyses are performed on data from numerical simulations of turbulence under fixed flow conditions, where it is frequently intractable to generate a sufficient number of truly independent realisations. In contrast, acquiring new realisations by running additional experiments often comes at a minimal incremental expense.

Results for the first three Fourier modes $m = 0, 1, 2$ has been presented in this study. The axial velocity PODs for the dominant $m = 1$ Fourier mode consist of helical structures and appear in opposite-chirality pairs. This characteristic has been observed for all three studied Reynolds numbers. The first two POD modes are similar in shape but have an opposite sense of rotation, which corroborates previously observed findings in experiments (Yoda *et al.* 1994; Gamard *et al.* 2004; Iqbal & Thomas 2007; Tinney *et al.* 2008*a*) and direct numerical simulations (Mullyadzhanov *et al.* 2018) in the far-field. Our study thus confirms the prevailing understanding that the helical mode dominates in the far-field of a turbulent jet. The dominant helical shapes also associate well with the helical ejections of coherent structures visualised by iso-surfaces of the vorticity magnitude. The POD structures corresponding to the radial velocity are helical as well, but exhibit a noticeably smaller helix angle. The current volumetric data enabled us, for the first time, to explore the characteristic vorticity structures in the self-similar region. It revealed the most dominant azimuthal vorticity structures as rings for $m = 0$ (the axisymmetric case) and C-shaped structures for $m = 1$. The C-shaped structures were accompanied by twisted tubular structures close to the jet axis for all three studied Reynolds numbers. Corrugations that appear on the surface of the tubular structures are constituted from several connected C-shaped loops around the axis. It is interesting to note that the helical twist, observed for the velocity structures, also manifests in vorticity loops. This latter feature becomes clear from the reconstruction of the data with many modes wherein these axial tubes break down into mere C-loops around the jet axis. The conical axial vorticity structures exhibit inclined streaks in the constant-θ-plane.

The phase analysis of the time coefficients associated with the first five POD modes uncovered that the characteristic Strouhal number ($St = fD/V_j$) of the velocity modes varies in the range $0.04 \lesssim St \lesssim 0.07$ for $m = 1{-}9$. Mullyadzhanov *et al.* (2018) reported that the mirror modes ($n = 1, 2$) for $m = 1$ had the same characteristic frequency with $St = 0.05$, based on a DNS of a jet with a co-flow. Their computation of St from a temporal coefficient analysis agreed well with local linear stability results. We determine the corresponding value to be approximately 0.05 for $n = 1, 2$ modes, but observe that the $n = 2$ mode has a slightly higher characteristic frequency than the $n = 1$ mode. However, the vorticity modes showed a characteristic Strouhal number of $St = 0.05 \lesssim St \lesssim 0.08$ for $m = 1{-}9$ and $n = 1{-}5$. Similar to the velocity structures, the primary and secondary vorticity POD C-structures for $m = 1$ also exhibit an opposite direction of rotation. From these phases plots, we can extract the rotation frequency of the POD modes, as they advect with the mean flow. The rotation of these structures is very evident from the time evolution of the reconstructed fields, as shown in the video included in the Supplementary movie 4. Furthermore, the temporal evolution of the reduced-order reconstructions, using only the dominant POD modes, uncovered the induction of axial velocity structures by the azimuthal vorticity structures in the first and second Fourier modes. As one would expect, the reconstructions showed that the strongest azimuthal vorticity induces sheets of axial velocity fluctuations in the far-field. The relationship between velocity and vorticity modes becomes evident from a comparison of the phase of the temporal coefficients of the temporal modes. The corresponding dominant modes of velocity and vorticity

are either perfectly in-phase or show a shift of π. In other words, corresponding POD modes of velocity and vorticity can be observed with the same or an opposite direction of rotation.

As the image-based Tomo-PIV technique produces a finite time-series length, it is mandatory to assess the convergence of the modal structures in light of possibly insufficient data. To this end, we used the sum of singular values $\Sigma_i \sigma_i$ of the data matrix, a measure of linear independence of the processed snapshots. The rapid convergence of this statistic, for different time-series durations, showed that the statistics used in our modal analysis is sufficiently converged.

Many tools introduced in this present analysis, such as the averaging across various experimental realisations by phase-synchronisation and the objective assessment of the information content in the gathered data, together with a modal decomposition of the flow field data, carry beyond our application and are valuable procedures for gaining insight into the essential and intrinsic physical mechanisms of turbulent flows.

Supplementary movies. Supplementary movies are available at https://doi.org/10.1017/jfm.2025.10786.

Funding. This study was supported by King Abdullah University of Science and Technology (KAUST) under BAS/1/1352-01-01.

Declaration of interests. The authors report no conflict of interest.

Appendix A. Photograph of experimental set-up

Figure 20 displays the experimental set-up with the camera arrangement.

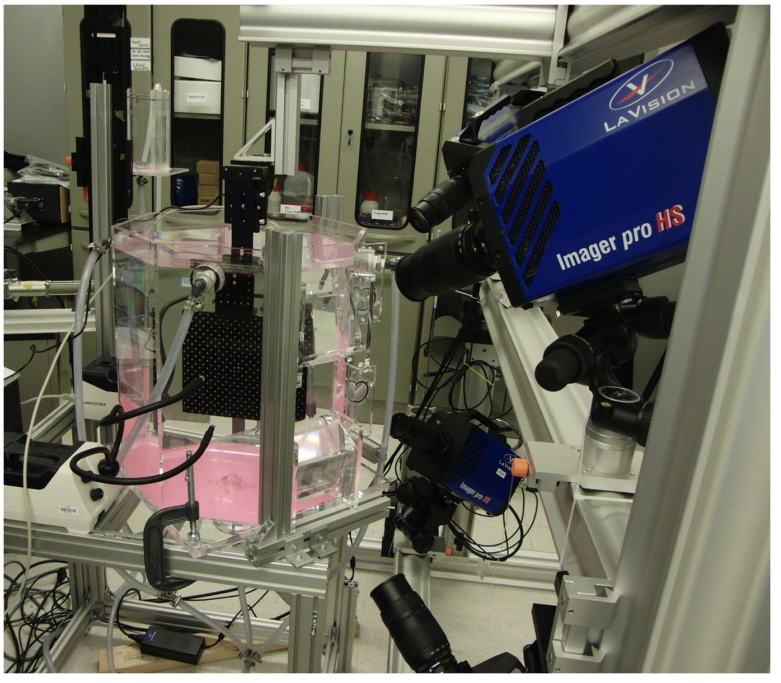

Figure 20. Photograph of the experimental set-up with the camera arrangement. The calibration plate is moved in the measurement region inside the octagonal tank using a motorised linear traverse. The four high-speed video cameras are focused on the measurement region with lenses mounted on Scheimpflug attachments. Two water-filled prisms, visible on the right-hand side of the tank, are implemented to minimise optical distortions.

Appendix B. Snapshot data matrix

Here, we show the snapshot data matrix with the fluctuating velocity field $\boldsymbol{f}$ in Fourier space. The three components are represented by the different colours. The variables of the cylindrical coordinates fall within the intervals $r = [r_1, r_{mx}]$, where r_1 is positive and nearly zero, and $z = [z_1, z_{mx}]$. The contribution from each point is weighed by the square root of its discrete control volume $\Delta V_j = r_j \Delta r \Delta z$.

$$\mathcal{D}^m(r, z, t) = \begin{bmatrix} f^m_{u_r}(r_1, z_1, t_1)\sqrt{\Delta V_1} & f^m_{u_r}(t_2)\sqrt{\Delta V_1} & \dots & f^m_{u_r}(t_N)\sqrt{\Delta V_1} \\ f^m_{u_r}(r_2, z_1, t_1)\sqrt{\Delta V_2} & f^m_{u_r}(t_2)\sqrt{\Delta V_2} & \dots & f^m_{u_r}(t_N)\sqrt{\Delta V_2} \\ \dots & \dots & \dots & \dots \\ f^m_{u_r}(r_{mx}, z_{mx}, t_1)\sqrt{\Delta V_{mx}} & f^m_{u_r}(t_2)\sqrt{\Delta V_{mx}} & \dots & f^m_{u_r}(r_{mx}, z_{mx}, t_N)\sqrt{\Delta V_{mx}} \\ f^m_{u_\theta}(r_1, z_1, t_1)\sqrt{\Delta V_1} & f^m_{u_\theta}(t_2)\sqrt{\Delta V_1} & \dots & f^m_{u_\theta}(t_N)\sqrt{\Delta V_1} \\ f^m_{u_\theta}(r_2, z_1, t_1)\sqrt{\Delta V_2} & f^m_{u_\theta}(t_2)\sqrt{\Delta V_2} & \dots & f^m_{u_\theta}(t_N)\sqrt{\Delta V_2} \\ \dots & \dots & \dots & \dots \\ f^m_{u_\theta}(r_{mx}, z_{mx}, t_1)\sqrt{\Delta V_{mx}} & f^m_{u_\theta}(t_2)\sqrt{\Delta V_{mx}} & \dots & f^m_{u_\theta}(t_N)\sqrt{\Delta V_{mx}} \\ f^m_{u_z}(r_1, z_1, t_1)\sqrt{\Delta V_1} & f^m_{u_z}(t_2)\sqrt{\Delta V_1} & \dots & f^m_{u_z}(t_N)\sqrt{\Delta V_1} \\ f^m_{u_z}(r_2, z_1, t_1)\sqrt{\Delta V_2} & f^m_{u_z}(t_2)\sqrt{\Delta V_2} & \dots & f^m_{u_z}(t_N)\sqrt{\Delta V_2} \\ \dots & \dots & \dots & \dots \\ f^m_{u_z}(r_{mx}, z_{mx}, t_1)\sqrt{\Delta V_{mx}} & f^m_{u_z}(t_2)\sqrt{\Delta V_{mx}} & \dots & f^m_{u_z}(t_N)\sqrt{\Delta V_{mx}} \end{bmatrix} \tag{B1}$$

Appendix C. Distribution of λ_n for different cases

Figure 21 depicts the distributions of λ for velocity and vorticity fields for azimuthal wavenumber $m = 1$ for the three different Reynolds number cases.

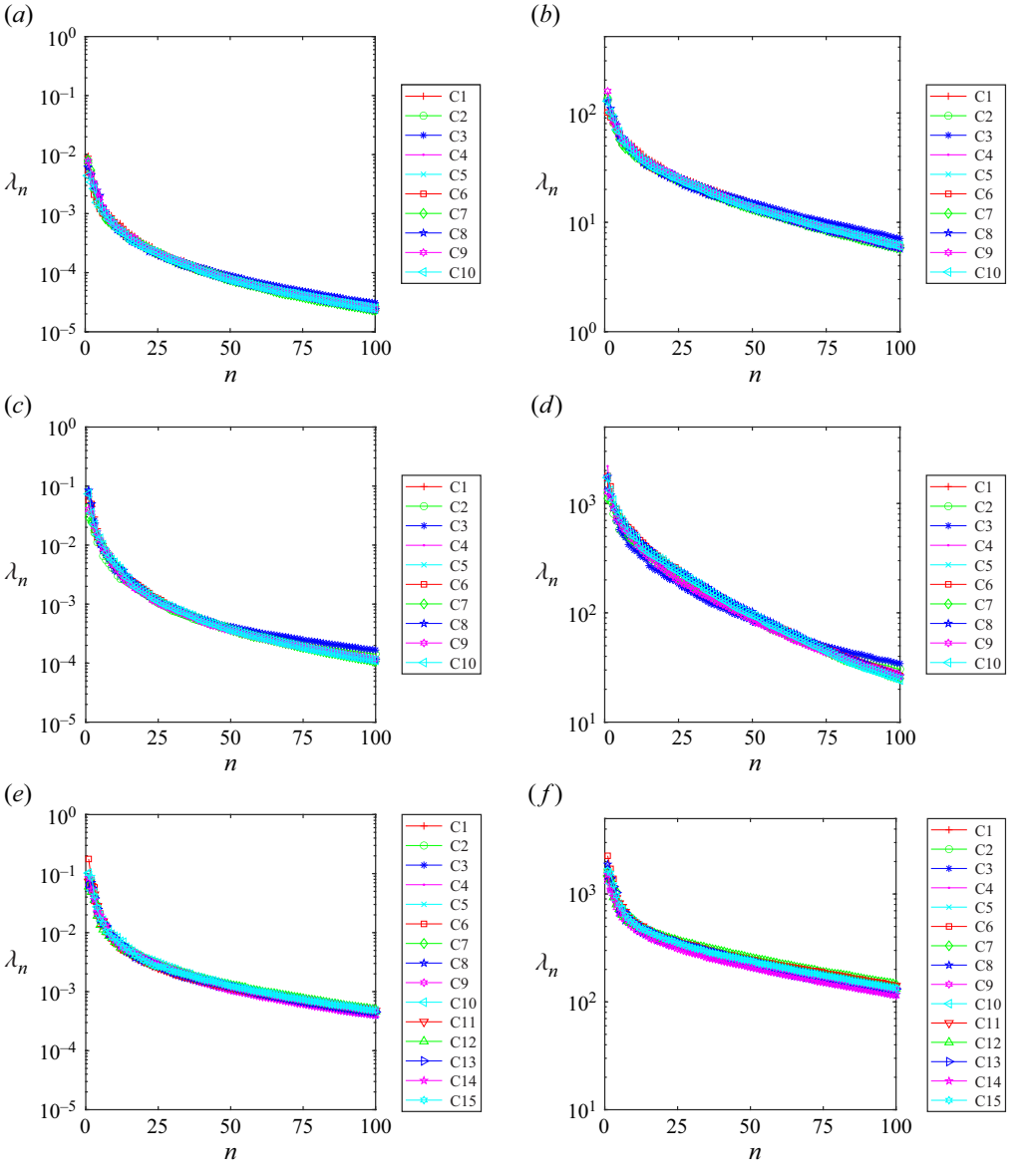

Figure 21. Distribution of λ for (a,c,e) velocity and (b,d,f) vorticity fields for $m = 1$ with different realisations for (a,b) $Re2K$, (c,d) $Re5K$ and (e,f) $Re10K$. Here, C1–C15 refers to independent experimental realisations. There are ten runs each for cases $Re2K$ and $Re5K$, and 15 runs for the case $Re10K$.

Appendix D. Decay constant and spreading rate

Figure 22 shows the axial dependence of the ratio $V_j/\langle U_{zc}\rangle$ as well as the jet half-radius for the *Re*5K case.

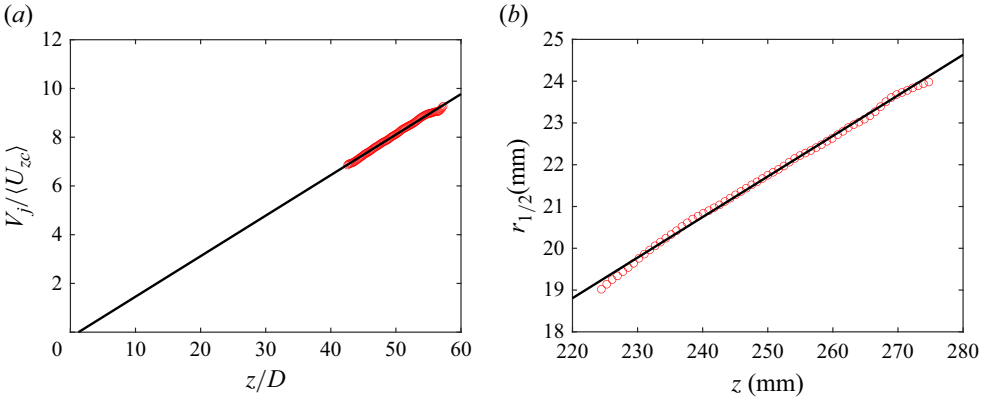

Figure 22. (*a*) Axial variation of the ratio, $V_j/\langle U_{zc}\rangle$ and (*b*) jet half-radius for *Re*5K. The red circles represent the current data and the black line is the linear fit. The slope of the line in panel (*a*) is the decay constant B_u; and the slope of the line in panel (*b*) gives the spreading rate $S = \mathrm{d}r_{1/2}/\mathrm{d}z$.

Appendix E. Axial variation of Kolmogorov scale

Figure 23 illustrates the variation of the Kolmogorov scale along the jet axis.

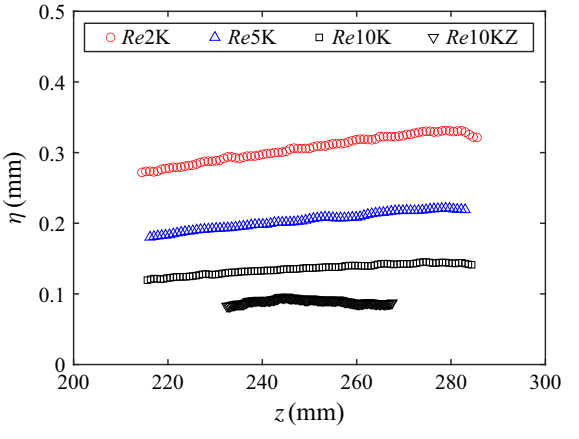

Figure 23. Axial variation of the Kolmogorov scale along the jet axis. Here, *Re*10KZ corresponds to experiments performed at 2.25× magnification with $Re = 10\,700$.

Appendix F. Reconstruction with different number of modes

Figure 24 presents visualisations of instantaneous reconstructed flow fields for the axial velocity and axial vorticity components. An azimuthal wavenumber of $m = 1$ for the $Re5K$ case has been chosen.

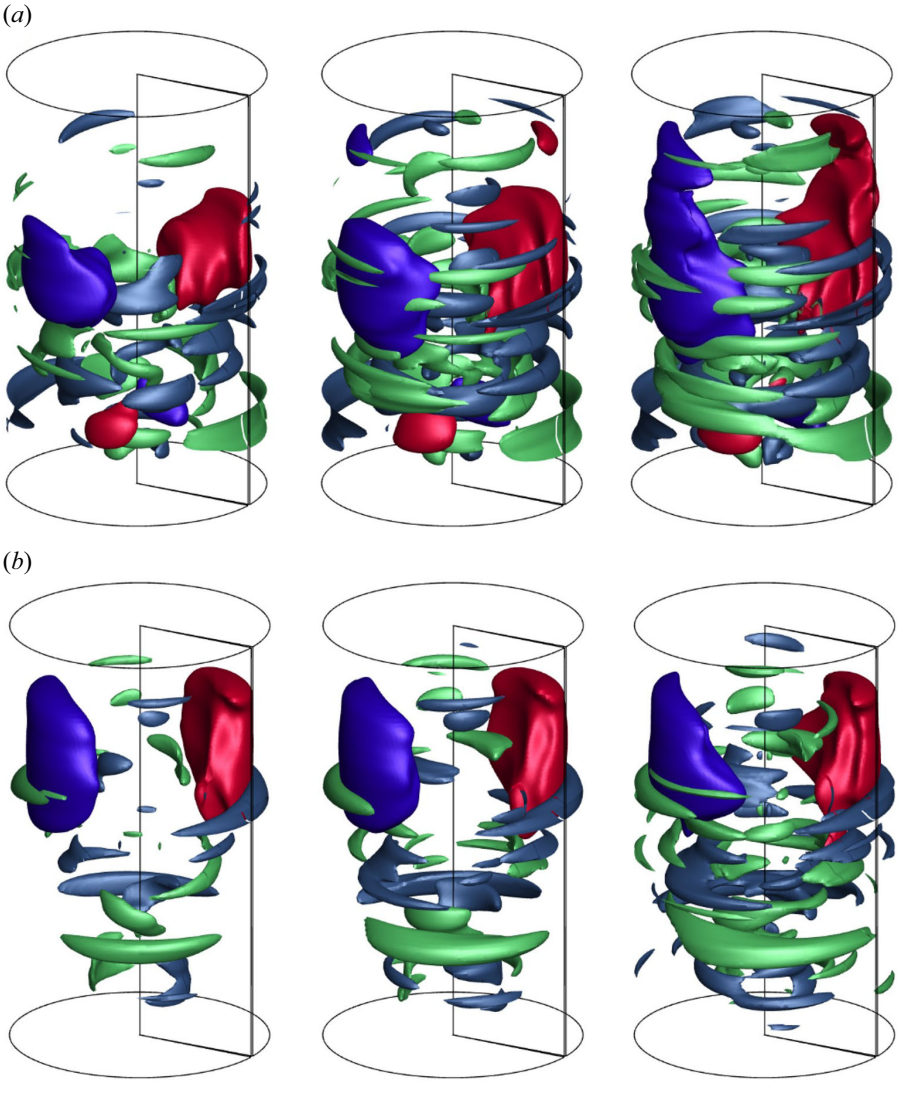

Figure 24. Instantaneous reconstructed images of u_z superimposed on ω_z for $m = 1$ for $Re5K$ with different number of modes contributing to 60 % (left), 70 % (middle) and 80 % (right) of the energy and enstrophy. Panels (*a*) and (*b*) correspond to two different time instants in the time evolution. Refer to figure 18(*c*) for the contour legend.

Appendix G. Phase of velocity and vorticity modes

Figure 25 compares the time coefficients of the first and second POD modes of velocity and vorticity.

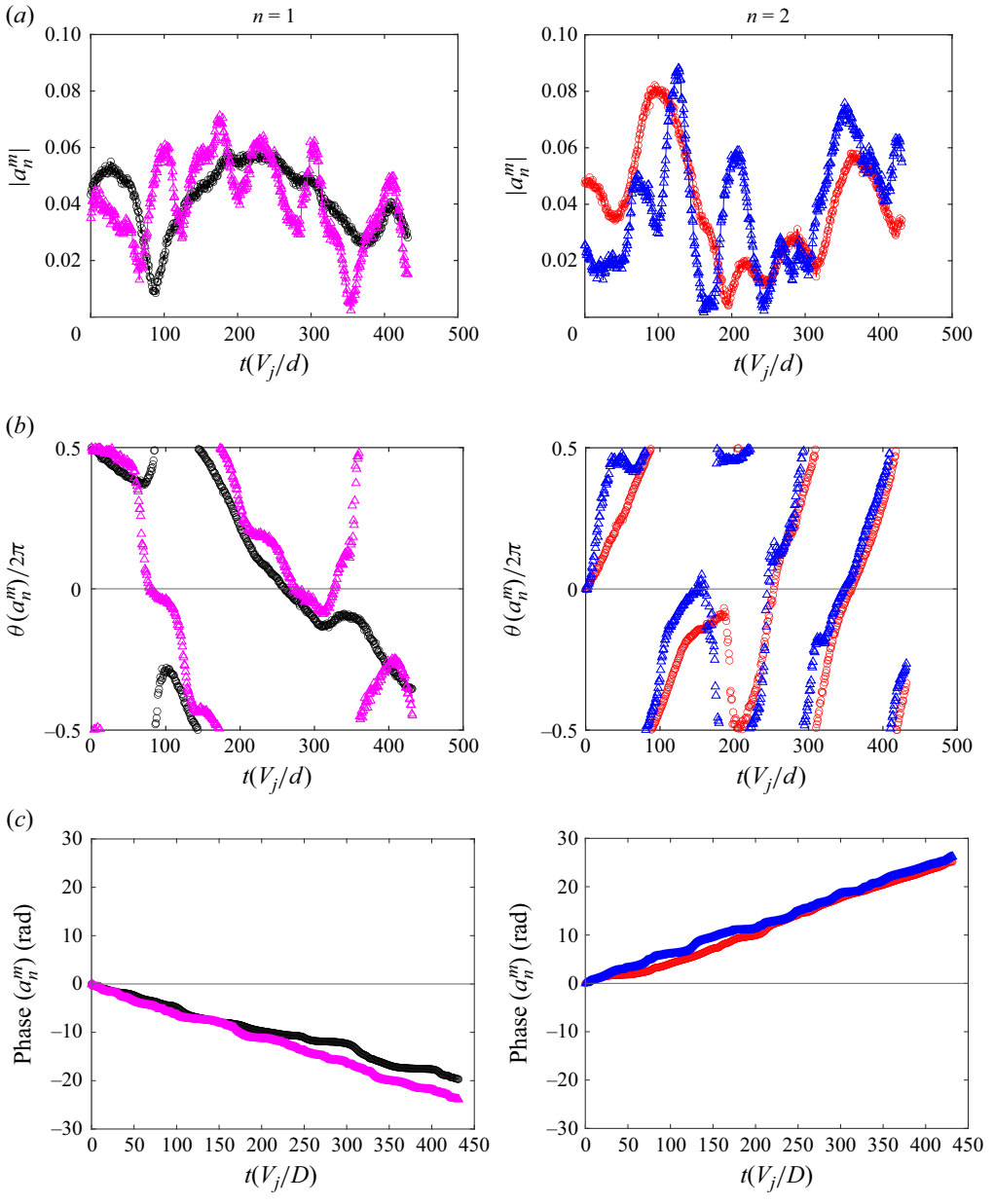

Figure 25. Comparison of the (*a*) magnitude $|a_n^m|$, (*b*) phase $\theta(a_n^m)$ and (*c*) cumulative phase of the time coefficient $a_n^m(t)$ corresponding to $n = 1$ and $n = 2$ modes of velocity and vorticity for $m = 1$ and Re5K. Modes of velocity and vorticity are represented by circles (in black and red) and triangles (in magenta and blue), respectively. The plot corresponds to the experimental run, whose reconstruction is shown in figure 18(*c*).

References

Alhareth, A.A., Mugundhan, V., Langley, K.R. & Thoroddsen, S.T. 2024*a* Coherent turbulent structures in a rapid contraction. *J. Fluid Mech.* **1000**, A63.

Alhareth, A.A., Mugundhan, V., Langley, K.R. & Thoroddsen, S.T. 2024*b* Turbulent structure and circulation inside different planar contractions. *Phys. Fluids* **36** (7), 075129.

Casey, T.A., Sakakibara, J. & Thoroddsen, S.T. 2013 Scanning tomographic particle image velocimetry applied to a turbulent jet. *Phys. Fluids* **25** (2), 025102.

Citriniti, J.H. & George, W.K. 2000 Reconstruction of the global velocity field in the axisymmetric mixing layer utilizing the proper orthogonal decomposition. *J. Fluid Mech.* **418**, 137–166.

Crow, S.C. & Champagne, F.H. 1971 Orderly structure in jet turbulence. *J. Fluid Mech.* **48** (3), 547–591.

Davoust, S., Jacquin, L. & Leclaire, B. 2012 Dynamics of $m = 0$ and $m = 1$ modes and of streamwise vortices in a turbulent axisymmetric mixing layer. *J. Fluid Mech.* **709**, 408–444.

Dimotakis, P.E., Miake-Lye, R.C. & Papantoniou, D.A. 1983 Structure and dynamics of round turbulent jets. *Phys. Fluids* **26** (11), 3185–3192.

Duggleby, A., Ball, K.S., Paul, M.R. & Fischer, P.F. 2007 Dynamical eigenfunction decomposition of turbulent pipe flow. *J. Turbul.* **8**, N43.

Duraisamy, K., Iaccarino, G. & Xiao, H. 2019 Turbulence modeling in the age of data. *Annu. Rev. Fluid Mech.* **51**, 357–377.

Elsinga, G.E., Scarano, F., Wieneke, B. & van Oudheusden, B.W. 2006 Tomographic particle image velocimetry. *Exp. Fluids.* **41** (6), 933–947.

Elsinga, G.E., Wieneke, B., Scarano, F. & Schröder, A. 2008 *Tomographic 3D-PIV and Applications*. Springer, pp. 103–125.

Gamard, S., Jung, D. & George, W.K. 2004 Downstream evolution of the most energetic modes in a turbulent axisymmetric jet at high Rreynolds number. Part 2. The far-field region. *J. of Fluid Mech.* **514**, 205–230.

Ganapathisubramani, B., Hutchins, N., Hambleton, W.T., Longmire, E.K. & Marusic, I. 2005 Investigation of large-scale coherence in a turbulent boundary layer using two-point correlations. *J. Fluid Mech.* **524**, 57–80.

Ganapathisubramani, B., Lakshminarasimhan, K. & Clemens, N.T. 2007 Determination of complete velocity gradient tensor by using cinematographic stereoscopic PIV in a turbulent jet. *Expt. Fluids* **42** (6), 923–939.

Glauser, M.N., Leib, S.J., George, W.K., 1987 Coherent structures in the axisymmetric turbulent jet mixing layer, W. In *Turbulent Shear Flows 5* (ed. F. Durst, B.E. Launder, J.L. Lumley, F.W. Schmidt & J.H. Whitelaw), pp. 134–145.Springer Berlin Heidelberg.

Head, M.R. & Bandyopadhyay, P. 1981 New aspects of turbulent boundary-layer structure. *J. Fluid Mech.* **107**, 297–338.

Hodžić, A., Olesen, P.J. & Velte, C. 2024 On the discrepancies between POD and fourier modes on aperiodic domains. *J. Engng Maths* **145**, 10.

Hori, T. & Sakakibara, J. 2004 High-speed scanning stereoscopic PIV for 3D vorticity measurement in liquids. *Meas. Sci. Tech.* **15** (6), 1067–1078.

Hussein, H.J. & George, W.K. 1990 Locally axisymmetric turbulence. Turbulence Research Laboratory, University at Buffalo, SUNY, Tech. Rep. 122.

Ianiro, A., Lynch, K.P., Violato, D., Cardone, G. & Scarano, F. 2018 Three-dimensional organization and dynamics of vortices in multichannel swirling jets. *J. Fluid Mech.* **843**, 180–210.

Iqbal, M.O. & Thomas, F.O. 2007 Coherent structure in a turbulent jet via a vector implementation of the proper orthogonal decomposition. *J. Fluid Mech.* **571**, 281–326.

Jordan, P. & Colonius, T. 2013 Wave packets and turbulent jet noise. *Annu. Rev. Fluid Mech.* **45** (2013), 173–195.

Jung, D., Gamard, S. & George, W.K. 2004 Downstream evolution of the most energetic modes in a turbulent axisymmetric jet at high reynolds number. Part 1. The near-field region. *J. of Fluid Mech.* **514**, 173–204.

Liepmann, D. & Gharib, M. 1992 The role of streamwise vorticity in the near-field entrainment of round jets. *J. Fluid Mech.* **245**, 643–668.

Lumley, J.L. 1967 The structure of inhomogeneous turbulent flows. in proc. intl colloq. on fine scale structure of the atmosphere and its influence on radio waves (ed. A.M. Yaglam & V.I. Tatarsky). *Doklady Akademii Nauk SSSR, Moscow* **Nauka**, 166–178.

Lumley, J.L. 1970 *Stochastic Tools in Turbulence*. Academic Press.

Marusic, I. 2001 On the role of large-scale structures in wall turbulence. *Phys. Fluids* **13** (3), 735–743.

MATSUDA, T. & SAKAKIBARA, J. 2005 On the vortical structure in a round jet. *Phys. Fluids* **17** (2), 025106.
MCKEON, B.J. & SHARMA, A.S. 2010 A critical-layer framework for turbulent pipe flow. *J. Fluid Mech.* **658**, 336–382.
MCNUTT, M.K., CAMILLI, R., CRONE, T.J., GUTHRIE, G.D., HSIEH, P.A., RYERSON, T.B., SAVAS, O. & SHAFFER, F. 2012 Review of flow rate estimates of the *Deepwater Horizon* oil spill. *PNAS* **109** (50), 20260–20267.
MUGUNDHAN, V., PUGAZENTHI, R.S., SPEIRS, N.B., SAMTANEY, R. & THORODDSEN, S.T. 2020 The alignment of vortical structures in turbulent flow through a contraction. *J. Fluid Mech.* **884**, A5.
MUGUNDHAN, V. & THORODDSEN, S.T. 2023 Circulation in turbulent flow through a contraction. *J. Turbul.* **24** (11-12), 577–612.
MULLYADZHANOV, R., ABDURAKIPOV, S. & HANJALIĆ, K. 2017 Helical structures in the near field of a turbulent pipe jet. *Flow, Turbul. Combust.* **98** (2), 367–388.
MULLYADZHANOV, R.I., SANDBERG, R.D., ABDURAKIPOV, S.S., GEORGE, W.K. & HANJALIĆ, K. 2018 Propagating helical waves as a building block of round turbulent jets. *Phys. Rev. Fluids* **3**, 062601.
OTTO, S.E. & ROWLEY, C.W. 2019 Linearly recurrent autoencoder networks for learning dynamics. *SIAM J. Appl. Dyn. Syst.* **18** (1), 558–593.
PANCHAPAKESAN, N.R. & LUMLEY, J.L. 1993 Turbulence measurements in axisymmetric jets of air and helium. Part 1. Air jet. *J. Fluid Mech.* **246**, 197–223.
PHILIP, J. & MARUSIC, I. 2012 Large-scale eddies and their role in entrainment in turbulent jets and wakes. *Phys. Fluids* **24** (5), 055108.
POPE, S.B. 2000 *Turbulent Flows*. Cambridge University Press.
SAMIE, M., APARECE-SCUTARIU, V., LAVOIE, P., SHIN, D.-H. & POLLARD, A. 2022 Three-dimensional large-scale and very-large-scale coherent structures in a turbulent axisymmetric jet. *J. Fluid Mech.* **948**, A29.
SCHMID, P.J. 2010 Dynamic mode decomposition of numerical and experimental data. *J. Fluid Mech.* **656**, 5–28.
SCHMID, P.J. 2022 Dynamic mode decomposition and its variants. *Annu. Rev. Fluid Mech.* **54** (1), 225–254.
SCHMID, P.J., VIOLATO, D. & SCARANO, F. 2012 Decomposition of time-resolved tomographic PIV. *Exp. Fluids.* **52** (6), 1567–1579.
SCHMIDT, O.T., TOWNE, A., RIGAS, G., COLONIUS, T. & BRÈS, G.A. 2018 Spectral analysis of jet turbulence. *J. Fluid Mech.* **855**, 953–982.
SCHRÖDER, A., GEISLER, R., ELSINGA, G.E., SCARANO, F. & DIERKSHEIDE, U. 2008 Investigation of a turbulent spot and a tripped turbulent boundary layer flow using time-resolved tomographic PIV. *Exp. Fluids.* **44** (2), 305–316.
SIROVICH, L., BALL, K.S. & KEEFE, L.R. 1990 Plane waves and structures in turbulent channel flow. *Phys. Fluids A: Fluid Dyn.* **2** (12), 2217–2226.
SUTO, H., MATSUBARA, K., KOBAYASHI, M., WATANABE, H. & MATSUDAIRA, Y. 2004 Coherent structures in a fully developed stage of a non-isothermal round jet. *Heat Transfer Asian Res.* **33** (5), 342–356.
TAIRA, K., BRUNTON, S.L., DAWSON, S.T.M., ROWLEY, C.W., COLONIUS, T., MCKEON, B.J., SCHMIDT, O.T., GORDEYEV, S., THEOFILIS, V. & UKEILEY, L.S. 2017 Modal analysis of fluid flows: an overview. *AIAA J.* **55** (12), 4013–4041.
TAIRA, K., HEMATI, M.S., BRUNTON, S.L., SUN, Y., DURAISAMY, K., BAGHERI, S., DAWSON, S.T.M. & YEH, C.-A. 2020 Modal analysis of fluid flows: applications and outlook. *AIAA J.* **58** (3), 998–1022.
TINNEY, C.E., GLAUSER, M.N. & UKEILEY, L.S. 2008*a* Low-dimensional characteristics of a transonic jet. Part 1. Proper orthogonal decomposition. *J. Fluid Mech.* **612**, 107–141.
TINNEY, C.E., UKEILEY, L.S. & GLAUSER, M.N. 2008*b* Low-dimensional characteristics of a transonic jet. Part 2. Estimate and far-field prediction. *J. Fluid Mech.* **615**, 53–92.
TOWNE, A., SCHMIDT, O.T. & COLONIUS, T. 2018 Spectral proper orthogonal decomposition and its relationship to dynamic mode decomposition and resolvent analysis. *J. Fluid Mech.* **847**, 821–867.
TSO, J. & HUSSAIN, F. 1989 Organized motions in a fully developed turbulent axisymmetric jet. *J. Fluid Mech.* **203**, 425–448.
VIOLATO, D. & SCARANO, F. 2013 Three-dimensional vortex analysis and aeroacoustic source characterization of jet core breakdown. *Phy. Fluids* **25** (1), 015112.
WESTERWEEL, J., ELSINGA, G.E. & ADRIAN, R.J. 2013 Particle image velocimetry for complex and turbulent flows. *Annu. Rev. Fluid Mech.* **45** (2013), 409–436.
WIENEKE, B. 2008 Volume self-calibration for 3D particle image velocimetry. *Exp. Fluids* **45** (4), 549–556.

WYGNANSKI, I. & FIEDLER, H. 1969 Some measurements in the self-preserving jet. *J. Fluid Mech.* **38** (3), 577–612.

YODA, M., HESSELINK, L. & MUNGAL, M.G. 1994 Instantaneous three-dimensional concentration measurements in the self-similar region of a round high-Schmidt-number jet. *J. Fluid Mech.* **279**, 313–350.